Au-doped PtAg nanorod array electrodes for proton-exchange membrane fuel cells

Fidiani, Elok; AlKahfi, Ahmad Zubair; Absor, Moh Adhib Ulil; Pravitasari, Ratna Deca; Damisih; Listiani Dewi, Eniya; Chiu, Yu-Lung; Du, Shangfeng

DOI:
10.1021/acsaem.2c02528

Au doped PtAg Nanorod Array Electrodes for Proton Exchange Membrane Fuel Cells

Elok Fidiani,[a,b] Ahmad Zubair AlKahfi,[c] Moh Adhib Ulil Absor,[c] Ratna Deca Pravitasari,[d] Damisih,[d] Eniya Listiani Dewi,[e] Gnanavel Thirunavukkarasu,[f] Yu-Lung Chiu,[f] Shangfeng Du[b]**

[a] Department of Physics, Parahyangan Catholic University, Jl. Ciumbuleuit 94, Bandung 40141, Indonesia

[b] School of Chemical Engineering, University of Birmingham, Birmingham, B15 2TT, U.K.

[c] Department of Physics, Universitas Gadjah mada, Kabupaten Sleman, Daerah Istimewa Yogyakarta 55281, Indonesia

[d] Research Center for Advanced Materials, National Research and Innovation Agency (BRIN), Building 224, Puspiptek, Tangerang Selatan 15314, Indonesia

[e] Research Center for Energy Conversion and Conservation, National Research and Innovation Agency (BRIN), Building 620, Puspiptek, Tangerang Selatan 15314, Indonesia

[f] School of Metallurgy and Materials, University of Birmingham, Birmingham, B15 2TT, U.K.

ABSTRACT

1D Pt-based alloy nanostructures have been demonstrated as highly active and durable catalysts for oxygen reduction reaction (ORR), which are the key to achieve the sustainability of proton exchange membrane fuel cells (PEMFCs). However, the high difficulty in the fabrication of a practical catalyst electrode based on these nanostructures has limited their potential for PEMFC applications. In this work, we demonstrate a facile approach of Pt alloy nanorod (NR) array gas diffusion electrodes (GDE) through in-situ grown on carbon paper gas diffusion layer and Au doping utilizing a one-step wet chemical reduction method. The GDE is directly used as the cathode in PEMFCs. The excellent catalytic acitivity of the Au doped PtAg NRs and the promoted mass transport characteristics of the array electrode structure enable an enhanced power density of 1.1-fold with an even 30 wt% less Pt loading, compared to the commercial Pt/C and Pt NR array GDEs. Density functional theory prediction reveals the increased ORR kinetic resulting from the weakening binding energy toward oxygen-containing species on the surface of Au doped PtAg. The Au stabilizing effect to minimize the atomic segregation between Pt and Ag is also investigated theoretically and experimentally based on the accelerated degradation test under the fuel cell operating condition.

KEYWORDS: PEMFC, catalyst, ORR, gas diffusion electrode, nanorod, Au doping, PtAg, PtAu

1. INTRODUCTION

Hybridization of Platinum (Pt) such as alloying with other metals has been intensively explored to enhance its catalytic performance toward oxygen reduction reaction (ORR) in proton exchange membrane fuel cells (PEMFCs), which offers an efficient, clean energy conversion to assist the transition to a low-carbon economy [1,2]. The formation of Pt-based hybrid catalysts is preferred not only to reduce the use amount of the scarce Pt but also to improve their ORR activities by lowering the activation energy at the cathode of the PEMFC [3,4]. The hybrid Pt-M nanocatalysts, such as PtCo [5–7], PtNi [8–10], PtFe [11–13], PtPd [14,15], PtAu [16,17], PtAg [18–20], etc., have been widely reported with their improved ORR activities in the literature. Currently, the hybrid PtCo/C has been used as the commercial catalyst in Toyota Mirai [21]. However, the durability issues remain as the major stumbling block to the sustainability of the PEMFC technology, which is mainly directed at the dissolution of catalyst nanoparticles (NPs) [22–24], corrosion of carbon support [25–27] and segregation of bimetallic Pt-M [28–30].

The shape-controlled nanostructures have been intensively explored to minimize the susceptibility of catalyst NPs toward dissolution. [31–33]. Theoretically, the catalyst with lower surface energy, defect-free crystal plane and preferential exposure of active sites such as a single-crystal one-dimensional (1D) nanostructure is a promising feature with enhanced catalytic activity [34–36]. Asymmetric single-crystal 1D nanostructures (e.g. nanowires (NWs) and nanorods (NRs)) are the ideal morphology to overcome the drawbacks of zero-dimension (0D) NP catalysts, specifically toward the dissolution and Ostwald ripening [34]. However, the small electrochemical surface area (ECSA) often limits the superiority of single-crystal 1D nanostructure catalysts as a consequence of their large bulk volume. To overcome this barrier, the preparation of such structures via hybridization has attracted a lot of efforts, which can potentially compensate for the

low ECSA with their extremely high surface activity, e.g., PtNi or PtCo NWs, or even ultrathin jagged Pt NWs by fully leaching Ni from the PtNi NWs [37,38]. Nevertheless, the technical difficulty to prepare these hybrid NWs, especially for scale-up production remains a major challenge. The requirement of a capping agent such as oleylamine (OAm) to finely controlled chemical reactions during the synthesis of 1D nanostructure potentially depresses their catalytic activity in fuel cells [39]. Until today, the fuel cell power densities reported for these highly active 1D nanostructures are still less than half of the latest Pt/C catalysts, and no results have been demonstrated for the jagged Pt nanowires in the fuel cell test [40].

Another challenge for the hybrid Pt-M nanostructures is rendered by the leaching of the alloyed metals and the atomic segregation due to the lattice mismatch with Pt, resulting in poor long-term stability during PEMFC operation [41,42]. The eminence of the Pt hybridization with other metals is mainly related to the surface property modification, which is caused by the change of the Pt-Pt bond distance and bonding interaction between Pt and the hybrid metals [43–45]. Herein, modification of these interactions is the key to stabilizing the Pt-M surface, which has been previously demonstrated through the doping method using stable metals such as gold (Au) [46–50]. The studies suggested that the presence of Au can weaken the binding of oxygen species on the Pt-M catalyst surface, suppressing the segregation of the alloyed metals and Pt [47–50].

In this work, we demonstrate a strategy for the GDE design with a unique catalyst layer structure based on Au doped PtAg NR arrays. The technique combines the support-free 1D nanostructures and hybridization of Pt and Ag, involving Au to mitigate the segregation and promote stability. The alloying with silver (Ag) is inspired by our previous work of AgPt NRs/C catalysts, demonstrating the enhanced catalytic performance toward ORR at the cathode of the PEMFC [50,51]. The theoretical study is also conducted for Au doping on 1D PtAg nanostructure catalysts through

density functional theory (DFT) calculation to get a better understanding of the ORR kinetic and the segregation phenomena of the Pt hybrid-based catalyst. The self-supported catalyst layer constructed from the PtAg-Au NR arrays takes the superiority of the 1D nanostructures and the elimination of carbon support to minimize the degradation mechanism. The extended active site exposure of the PtAg-Au NRs and the thin catalyst layer based on NR arrays with improved mass transfer performance is also the privilege of this unique electrode structure. Hence, improved power density and durability are demonstrated from the MEA test in PEMFC single cells.

2. EXPERIMENTAL SECTION

2.1. Material. All materials were used as received without additional treatment and purification, including 2-propanol (IPA) and ethanol purchased from Fisher Scientific, U.K, H_2PtCl_6 (8 wt% in H_2O), 0.1 M $AgNO_3$, $HAuCl_4.3H_2O$ and HCOOH (≥95%) (Sigma-Aldrich, U.K), Sigracet 39 BC carbon paper gas diffusion layer (GDL, Fuel Cell Store, USA) and 10 wt% Nafion® polymer dispersion (D1021) (Ion Power Inc., USA). Commercial gas diffusion electrode (GDEs, 0.2 mg_{Pt} cm^{-2}, Fuel Cell Store, USA) was employed as the anode, and Pt/C nanoparticle catalyst (46.2 wt% Pt, TEC10E50E, TKK, Japan) was used as the benchmark catalyst. The water used in this work was deionized (DI) to 18 MΩ cm using a Millipore water system (Milli-Q).

2.2. Fabrication of GDEs based on Pt and Pt-M NR arrays. Pt NR array GDE (0.4 mg_{pt} cm^2) was made by adapting the wet chemical reduction approach based on our previous work [54]. Before growing catalysts, a piece of 5 x 5 cm^2 GDL was first rinsed with H_2O and IPA, followed by soaking in H_2O. The GDL was then immersed in a square petri dish filled with 16.5 mL H_2O followed by adding 255 μL H_2PtCl_6 (8 wt% in H_2O) and 830 μL HCOOH during bath sonication for 1 minute. The reaction was then carried on at 40 °C for 72 hours (or until the solution was

colourless) to obtain the Pt NR array GDE. The approach was then modified to fabricate the PtAg NR array GDE (0.4 mg_{PtAg} cm^2) by adjusting the interval reaction time and the concentration of metal precursors with the atomic ratio of Pt : Ag = 7 : 3 as presented in Figure S1. It is crucial to control the reaction parameter by reducing Pt before adding Ag in order to obtain 1D nanostructures [51]. First, 200 μL H_2PtCl_6 (8 wt% in H_2O) and 830 μL HCOOH were added onto the petri dish where 5 x 5 cm^2 GDL was immersed in 16.5 mL H_2O. After the reacttiton was kept at 40 °C for 3 hours, 185 μL of 0.1 mol L^{-1} $AgNO_3$ was added during bath sonication for 1 minute, and then the reaction was continued at 40 °C. The colourless solution after a total reaction of ca. 72 hours indicates the complete reduction of Pt - Ag and the formation of PtAg NR arrays on the GDL. The same process was used to make 2 at% Au doped PtAg NR array GDE, but 60 μL 0.025 mol L^{-1} $HAuCl_4$ was added togetther with H_2PtCl_6 at the beginning, and only 162 μL 0.1 mol L^{-1} $AgNO_3$ solution was used. Before conducting the characterizations, all the as-made GDEs were washed with H_2O and IPA, followed by drying at 40 °C for 2 hours.

2.3. Physical characterization. Transmission electron microscopy (TEM) analysis was conducted on JEOL 1400 TEM, 80 kV, Japan to analyze the structure and morphology of the GDEs, along with high-resolution TEM (HR-TEM, Talos F200X, operated at 200 kV) equipped with Super-X EDS system with four silicon drift detectors (SDDs) (Bruker, USA). X-ray diffraction (XRD) analysis was performed with Bruker D8 Auto-sampler (USA) equipped with a Cu Kα X-Ray source (λ = 0.15406 nm). X-ray photoelectron spectroscopy (XPS, Thermo Fisher Scientific NEXSA spectrometer) with a micro-focused monochromatic Al $K\alpha$ source (72 W) was employed with the processing software of CasaXPS (version: 2.3.18PR1.0) and sample charging corrected using the C 1s peak at 284.8 eV as reference. The catalyst loading measurement was carried on using thermogravimetric analysis (TGA, NETZSCH TG209F1, Germany) and thte

metal content was evaluated using inductively coupled plasma mass spectrometry (ICP-MS, Perkin Elmer Nexion 300X, USA) (plasma strength of 1500 W).

2.4. Membrane Electrode Assembly (MEA) fabrication and fuel cell testing. The as-made GDEs were cut to 4 x 4 cm^2 as cathode and then coated with the ionomer solution with a Nafion loading of ca. 0.4 mg cm^{-2}. The coating solution was made by mixing 62.5 μL of 10 wt % Nafion and 0.2 mL of IPA, followed by bath sonication for 5 minutes. The coated 4 x 4 cm^2 cathode and anode were then assembled with a 6 × 6 cm^2 Nafion® 212 membrane by hot pressing under 4.9 MPa at 135 °C for 2 minutes. The membrane electrode assembly (MEA) was allowed to cool down at room temperature before testing in a PEMFC.

The MEA single-cell test was carried out on a Biologic-PaxiTech FCT-50S PEMFC test rig (France) with polytetrafluoroethylene (PTFE, 254 μm in thickness) gaskets used at both the anode and cathode sides. Membrane activation was first run by holding the cell potential at 0.6 V for ca. 10 hours under fully humidified H_2/Air at 80 °C and stoichiometric ratios of 1.3/1.5 with an absolute pressure of 1.5/1.5 bar_{abs} at the anode and cathode, respectively. The pressure was then changed to 2.5/2.3 bar_{abs} at the anode and cathode, respectively, followed by conducting the break-in procedure based on the EU harmonized protocols [55]. The polarization curve was then recorded between 0 – 2.0 A cm^{-2} with a step size of 0.02 A cm^{-2} (90-sec holding) for the low current density region between 0 – 0.1 A cm^{-2} and 0.1 A cm^{-2} (150-sec holding) for the remaining stepping point. Electrochemical impedance spectroscopy (EIS) analysis was then conducted at a low current density region of 30 mA cm^{-2} with the amplitude of 72 mA for the 16 cm^2 cell in the frequency range of 10 kHz – 0.1 Hz. Applying a Galvano EIS here is to anticipate the voltage fluctuation at the open-circuit voltage (OCV). The potentio EIS were then recorded at a fixed potential of 0.65 V and 0.5 V (medium and high current density, respectively), with an amplitude of 10 mV within

the same frequency range of 10 kHz – 0.1 Hz. This method was intended to anticipate the huge voltage drop before reaching a certain value at a high current density region. The cathode cyclic voltammogram (CV) was also recorded using the EZStat-Pro potentiostat (NuVant Systems Inc., USA) between 0.05-1.2 V with a scan rate of 20 mV s^{-1}. The testing was carried out at 80 °C under fully humidified H_2/N_2 of the anode/cathode with the stoichiometry ratios of 2/9.5 and absolute pressure of 1.5/1.5 bar_{abs}, respectively. The accelerated degradation test (ADT) of the cathode was conducted at the same condition using potential sweeping between 0.6-1.2 V at a scan rate of 100 mV s^{-1} for 5000 cycles.

3. RESULTS & DISCUSSION

3.1 Physical Characterization. TEM images in **Figure 1a-b** show the structure of Au doped PtAg arrays scrabed from the GDL surface. The average NR diameter is ~ 4 nm with a length of ca. 20 nm, which is also comparable to the size of the Pt-alloy NRs grown on the carbon support with a similar composition [50]. The crystallinity of the 1D nanostructure with a measured interplanar space of 0.23 nm is assigned to the Pt [111] crystal facets as shown in the HR-TEM image (**Figure 1c**), which also emphasizes the anisotropic growth of the NR along the <111> direction. The element mapping by STEM-EDX (**Figure 1d-g)** confirms the presence of Pt, Ag and Au, assigning the alloying formation within the NRs.

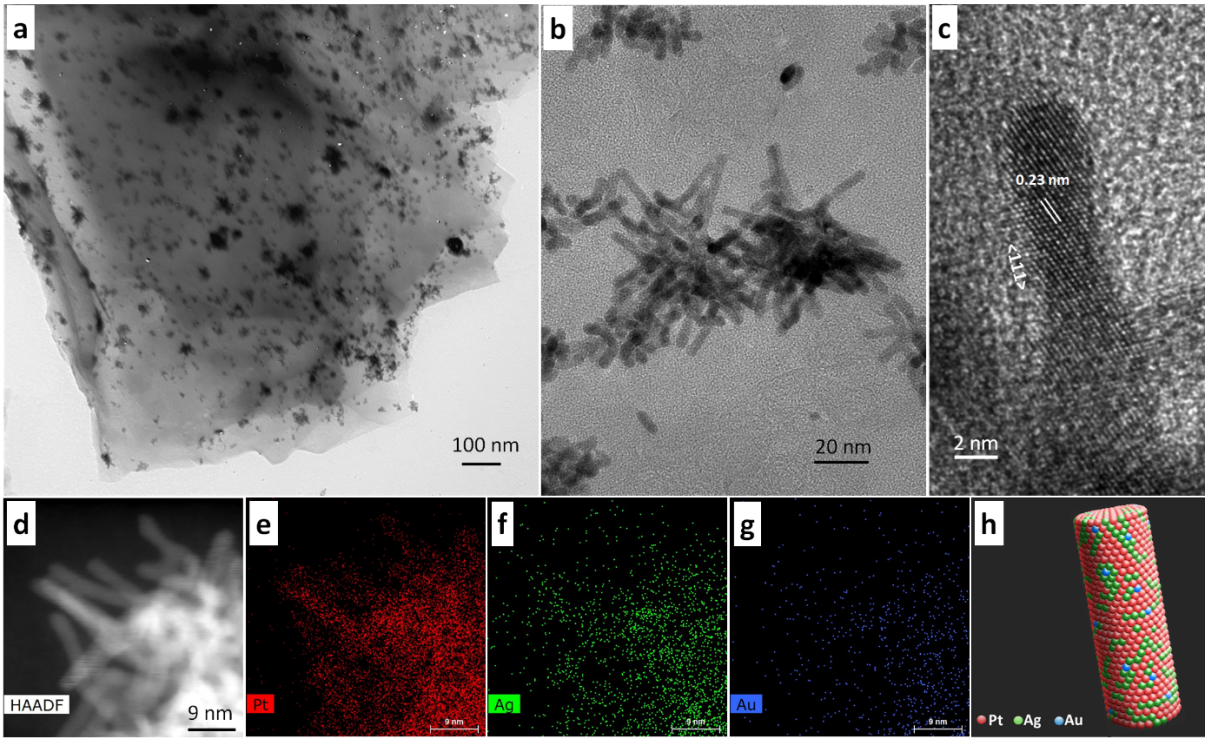

Figure 1. Images of PtAg-Au NR arrays scrabled from the GDE obtained by (a-b) TEM, (c) HR-TEM, (d-g) the element mapping by STEM-EDX. (h) a visualized structure of the PtAg-Au NR.

The XRD peaks in **Figure 2** are indexed to (111), (200), (220) and (311) planes, appointed to the face-centered cubic (FCC) crystal structure of bulk Pt (JCPDS-04-0802), Ag (JCPDS-04-0783) and Au (JCPDS: 04-0784), respectively. The high peak intensity at 26.6° is associated with the graphitic carbon of the GDL component as typically observed in the previous work employing the same GDL [56]. The peaks of the PtAg and PtAg-Au NR array GDEs exhibit a negative shift of ca. 0.1° compared to the Pt NR array GDE (**Figure 2**). The main (111) peak of the PtAg-Au NR is in alignment with the PtAg NR (**Figure 2b**), indicating a similar lattice space due to alloying with Ag. The PtAg-Au NR array GDE also shows a higher peak intensity for (111) than that of the PtAg NR array GDE, which potentially refers to the longer NRs and higher degree of crystallinity after the Au doping.

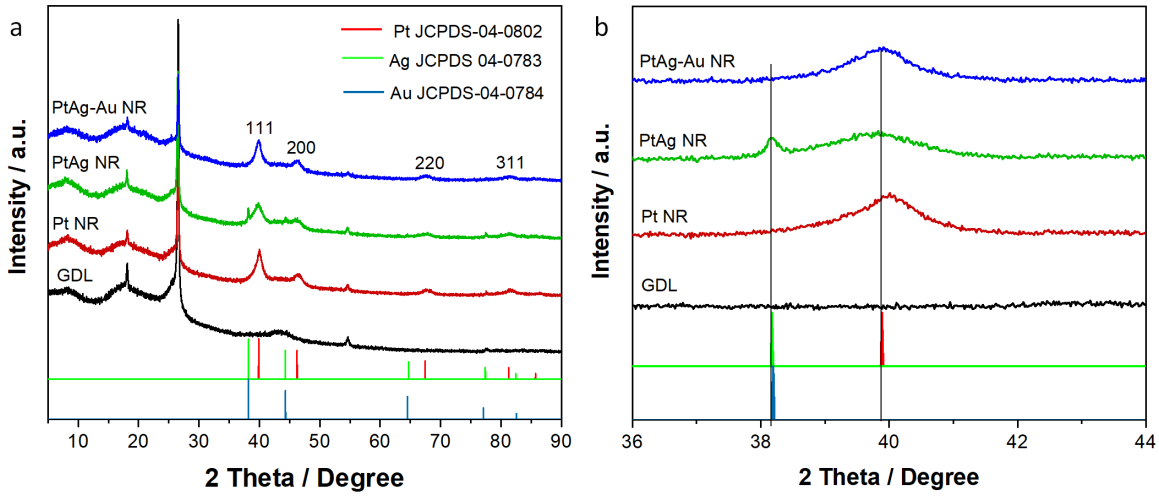

Figure 2. XRD patterns of the Pt NR, PtAg NR and PtAg-Au NR array GDEs and the GDL with the references of Pt, Ag and Au.

Generally, the structure of the Pt and PtAg NR array GDEs is similar (Figure S2), which is comparable to our previous works utilizing the preferential growth in a specific direction forming 1D nanostructures [51,54]. However, with a higher Ag content (Pt_1Ag_1 NR) the formation of the shorter NRs of ca. 10 nm are observed as shown in Figure S2. In agreement, the XRD analysis results (Figure S3) confirm the broadening Pt peaks with the increasing Ag loading of up to 50 at%, which can be ascribed to the domination of the shorter NRs especially in the Pt_1Ag_1 NR array GDE. Furthermore, the Ag peaks are detected and becoming more distinguished with the increasing Ag content, suggesting the presence of pure Ag phase than the Pt-Ag alloy on the GDL surface. Nevertheless, the Ag metal phase peaks are disappeared on the pattern of the PtAg-Au NR array GDE shown in **Figure 2**. This outcome suggests that the insertion of Au also effecttively improves the alloying degree of Ag with Pt.

TGA was employed to determine the metal loading of the GDEs (Table S1). A catalyst loading of 0.39 – 0.41 mg cm^{-2} is obtained for the three GDEs, which is in agreement with the theoretical

loading of 0.40 $mg_{catalyst}$ cm^{-2}. This result demonstrates the high efficiency for directly growing catalysts on the GDL surface by using this facile approach. ICP-MS analysis was also conducted to accurately quantify the metal content ratios with the GDEs, which detects 2.48 at% Au for the PtAg-Au NR array GDE (Table S1). Further evaluation by the XPS analysis reveals a significant change of the surface composition compared to the bulk elements (**Figure 3**). A very low Au concentration of ca. 0.3 at% is measured from the XPS survey scan in **Figure 3a**, suggesting that most Au are deposited beneath the surface of the NRs. The XPS analysis result shows 57.24 at% of Ag and 42.76 at% of Pt on the surface for the PtAg NR array GDE (Table S1). After alloying with ~2 at% of Au, Pt dominates the surface composition of 65.46 at%. These changes further confirm the effectiveness of Au alloying to control the arrangement of Pt and Ag along with the NR array GDE, resulting in a high Pt deposition on the NR surface.

The corresponding high-resolution XPS spectra of the Pt 4f and Ag 3d regions are shown in **Figure 3c-h**. Au 4f peaks are also detected for the PtAg-Au NR array GDE within the high-resolution Pt 4f region (**Figure 3g**). Compared to the Pt NR array GDE (**Figure 3c**), the Pt 4f peaks of the PtAg NR and PtAg-Au NR array GDEs (**Figure 3e, g**) shift more negatively (~ 0.2 eV), referring to the change of the Pt binding energy. This outcome confirms a similar change as before in the electronic structure of Pt because of the interaction with Ag/Au, inducing modification of the Pt surface after the formation of 1D Pt alloy nanostructures [19]. Similarly, Ag 3d peaks of the PtAg NR and PtAg-Au NR array GDEs are shifted negatively by about ~0.1 eV from the referenced Ag (**Figure 3d, f, h**), indicating charge transfer phenomena due to the formation of the bimetallic Ag and Pt alloy, causing the change of the binding energy of Ag^0 [57]. Furthermore, the peak fitting (blue circles) on the high-resolution Pt 4f and Ag 3d spectrum in **Figure 3g-h** show that PtAg-Au NR array GDE is entirely composed of Pt and Ag metallic states.

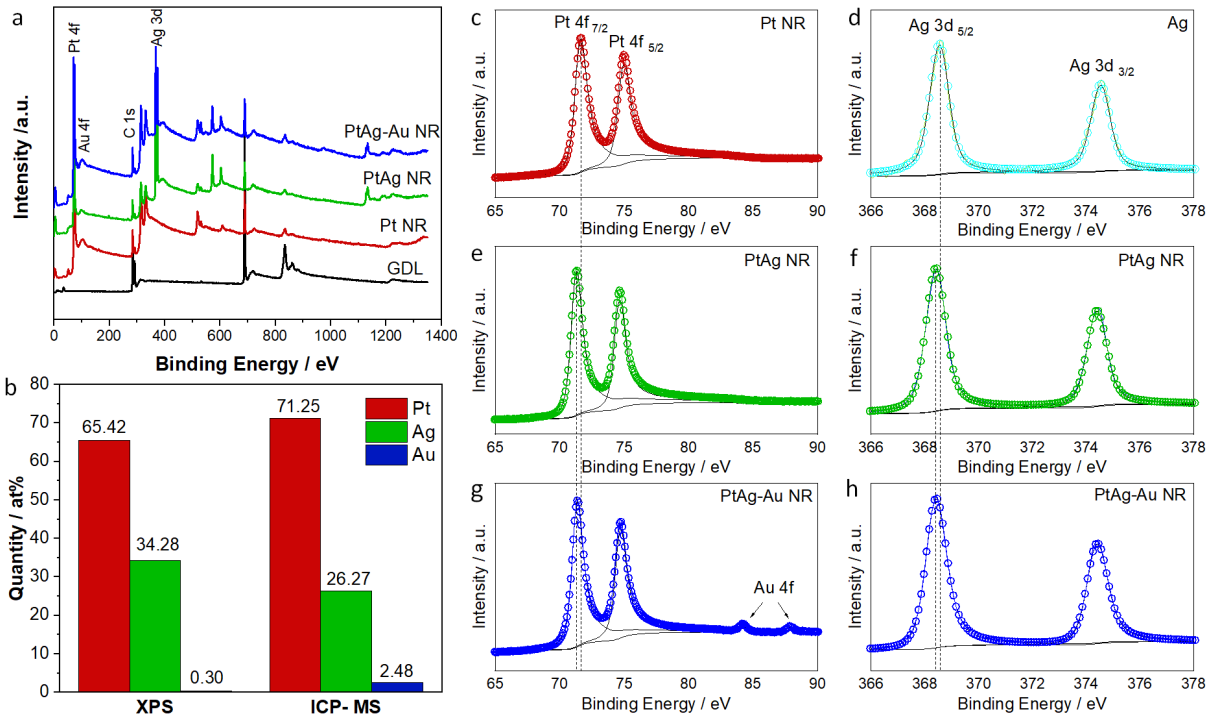

Figure 3. (a) XPS survey of the GDL, Pt NR, PtAg NR and PtAg-Au NR array GDEs, (b) comparison of quantitative measurement of PtAg-Au NR using XPS and ICP-MS analyses. (c-h) High-resolution XPS spectra of Pt 4f and Ag 3d regions of the as-made GDEs.

3.2. MEA Single-Cell Performance. The as-made GDEs were tested as cathodes in H_2/Air single cells along with the commercial Pt/C GDE as the benchmark, and the metal loading was set the same for all the GDEs at 0.4 mg_{metal} cm^{-2}. The polarization and power density curves were recorded under H_2/Air and are shown in **Figure 4a-b**. The power density trend of the GDEs at 0.6 V follows PtAg-Au NR > Pt NR > Pt/C > PtAg NR (**Figure 4c**). The peak power density of the PtAg-Au NR array GDE reaches 0.61 W cm^{-2}, which is slightly higher than that of the Pt NR array GDE (0.58 W cm^{-2}) and commercial Pt/C (0.56 W cm^{-2}). The result reveals the superiority of the PtAg-Au NR array GDE considering about 30 wt% less Pt within the catalysts than the GDE made of monometallic Pt NR array and Pt/C. Such an eminence is further confirmed after normalizing

to the Pt mass (Figure S5) showing that about 1.9 W mg_{Pt}^{-1} is achieved for the PtAg-Au NR array GDE compared to 1.35 and 1.25 W mg_{Pt}^{-1} for the Pt NR array and Pt/C GDEs. The power performance of the PtAg NR array GDE is relatively low, which can be ascribed to the relatively heavier agglomeration of the PtAg NRs and the lower Pt content within the catalyst in particular the high ratio of Ag distributed on the NR surface which further reduces the ORR catalytic activity. Due to the higher Pt content, the Pt NR array GDE still shows the best power performance at the high voltage region above 0.7 V, which is also demonstrated by the lowest impedance represented by the smallest semicircle diameter of the EIS spectra recorded at the low current density of 30 mA cm^{-2} (**Figure 4d**), but the PtAg-Au NR array GDE still shows a very close semicirle. The EIS recorded at 0.5 V shows the lowest impedance of the PtAg-Au array NR GDE (Figure S6b) due to the much-reduced mass transfer resistance, resulting from the good distribution of the NR arrays formed on the GDL surface as shown in **Figure 1a**. Therefore, the introduction of this small amount of Au improves the morphology, structure and distribution of the PtAg NR arrays, enhancing the intrinsic catalytic activity towards ORR. It also facilitates the mass and charges transfer characteristics during the fuel cell operation for a better power performance as further confirmed by MEA testing results in H_2/O_2 presented in Figure S8 and Table S2.

This improvement demonstrates a promising attempt on the Au insertion to optimize the 1D structure and atomic arrangement of Pt and its alloy for growing NR array GDEs. However, a higher amount of Au doping of about 5 at% results in decreased power performance for the PtAg-Au NR array GDE (Figure S9). Similar behavior is also observed from our previous work on carbon supported Au doped PtAg NR catalyst [50], which is rendered by the less favorable Au surface toward ORR [46].

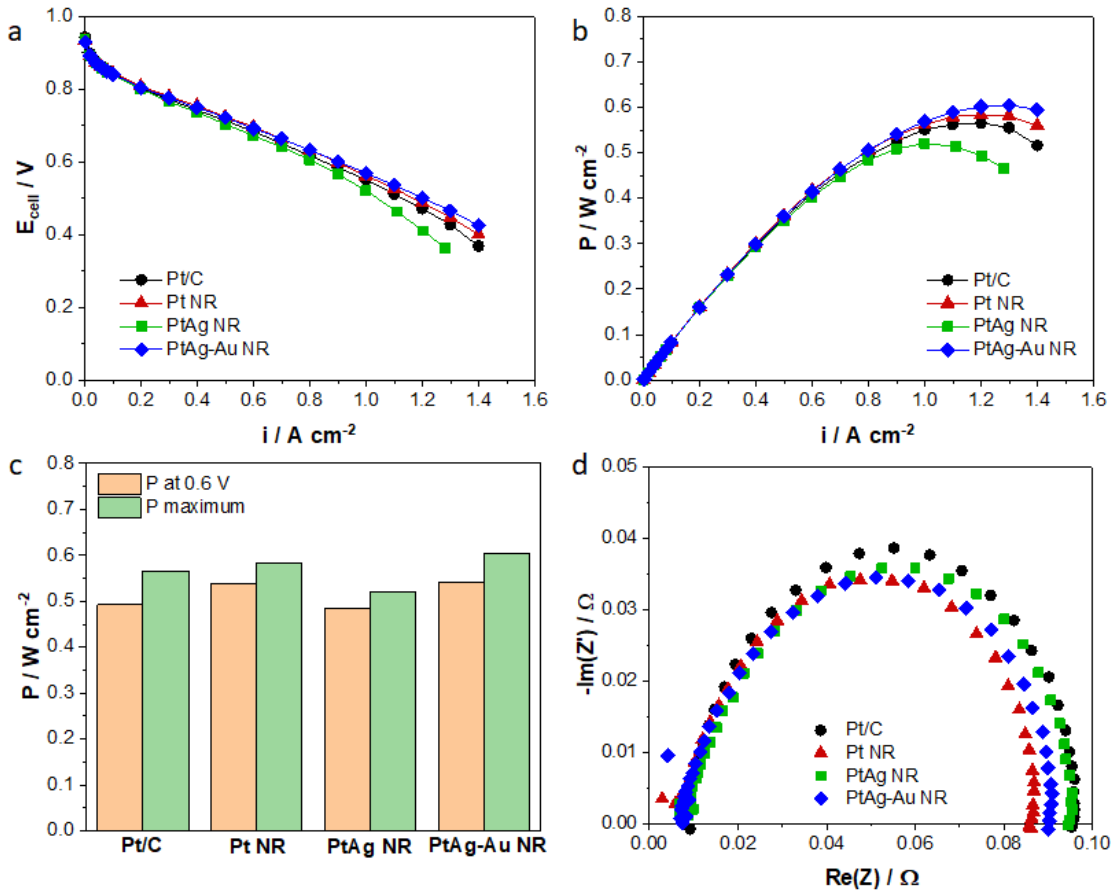

Figure 4. MEA testing results recorded under fully humidified H_2/air at the anode/cathode at 80 °C with stoichiometric ratios of 1.3/1.5 and absolute pressure of 2.5/2.3 bar_{abs}, respectively: (a) polarization and (b) power density curves of the commercial Pt/C, Pt NR, PtAg NR and PtAg-Au NR array GDEs. (c) Comparison of the corresponding peak and power density at 0.6 V and (d) the corresponding EIS spectra recorded at 30 mA cm^{-2}.

3.4. Accelerated Degradation Testing. The ADT was performed in single-cell PEMFCs to evaluate the durability of the GDEs. It was conducted with 5000 potential cycles between 0.6 – 1.2 V at a sweep rate of 100 mV s^{-1} under the N_2-saturated cathode with the hydrogen anode. As shown in **Figure 5**, the peak power density losses of the NR array GDEs after ADT are lower than that of the Pt/C GDE, even with Ag which has been considered a highly unstable element under

the acidic PEMFC operating conditions. This is mainly attributed to the anisotropic 1D nanostructure of the NRs and carbon support-free NR array GDE feature. The AgPt NR array GDE exhibits a larger decline ratio of 45.67% compared to 43.62% of the Pt NR array GDE, of course, due to the instability of Ag leading to the segregation of Ag and Pt. Nevertheless, such loss is prevented with the doping of 2 at% Au (PtAg-Au NR), endowing the lowest decline ratio of 37.09% after the ADT. It is even much lower than that of the monometallic Pt NR array GDE (43.62%), which further signifies the positive contribution of the Au doping towards electrode durability.

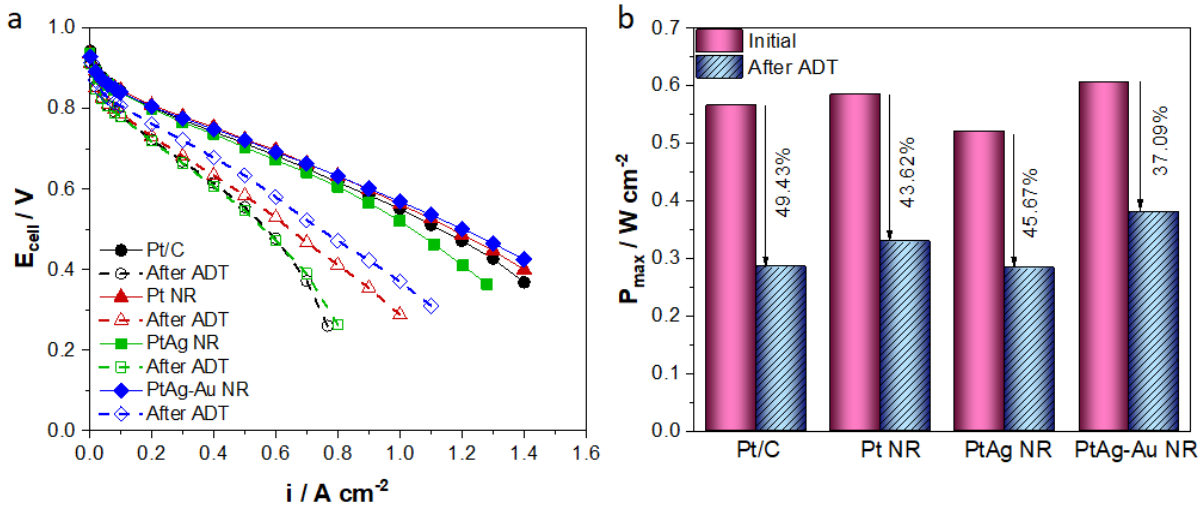

Figure 5. (a) Comparison of polarization curves and (b) the corresponding power density decline ratio from different GDEs after the ADT recorded under fully humidified H_2/air of the anode/cathode at 80 °C with the stoichiometric ratios of 1.3/1.5 and absolute pressure of 2.5/2.3 bar_{abs}, respectively.

The minimum power density decline of the PtAg-Au NR array GDE is related to the least ECSA loss, as presented in Figure S10. The trend of decreased ECSA values from the CVs is in agreement with the decline of the power performance output, suggesting the surface area loss is the main contributing factor to the poor ORR activity after the ADT. The larger ECSA decline with the Ag

is related to the stability of Ag in acidic media, which has also be reported in the previous works [51,58]. The ECSA loss of the PtAg NR array GDE after the ADT is reduced by ~14% with the presence of Au. This finding further suggests the stabilization effect of Au in minimizing the atomic segregation and surface oxidation during the potential cycling.

3.4. Density Functional Theory. The effect of Au doping on PtAg NR surface toward the ORR activity and durability is further investigated using the DFT calculation based on the norm-conserving pseudopotentials and optimized pseudoatomic localized basis function implemented in the OPENMX code [59–62]. The exchange-correlation functional was treated within the Perdew-Burke-Ernzerhof generalized-gradient approximation [63,64]. The basis function was expanded by a linear combination pseudoatomic orbital generated using a confinement scheme, where two *s*-, two *p*-, two *d*-, and one *f*- orbitals were used for the metal atoms (Pt, Ag, and Au) and two *s*-, two *p*-, two *d*-orbitals for the oxygen atom [60–62]. An energy cut-off of 350 eV was applied for the plane-wave expansion of the electronic eigenfunctions. A (3 × 3 × 1) Monkhorst-Pack mesh of *k* points was used to calculate geometries and total energies for the Brillouin zone integration.

The catalyst is constructed with a face-centered cubic Pt (111) surface composed of a hexagonal (3 × 3) surface unit cell with six atomic layers, each of which contained nine atoms, which is based on the (111) facet as confirmed by TEM and XRD analysis **(Figure 1** and **Figure 2)**. A periodic slab to model the surface was integrated, where a sufficiently large vacuum layer (20 Å) was applied in order to avoid the spurious interaction between slabs. The PtAg (111) surface was modelled by introducing Pt skin layers in the top three surface layers supported on a PtAg (111) substrate. While Au-doped Pt skin layers supported on the ordered PtAg (111) substrate were prepared by substituting a single Pt atom in each Pt skin layer with an Au atom. During the structural relaxation, the energy convergence criterion was set to 10^{-9} eV. The lattice and positions

of the atoms were optimized until the Hellmann-Feynman force components acting on each atom were less than 1 meV/Å.

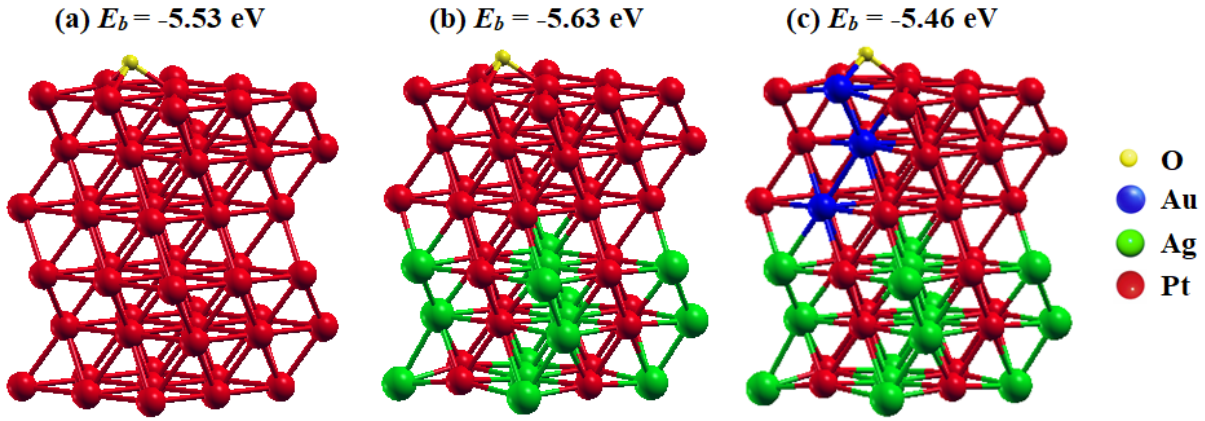

Figure 6. (a) Optimized atomic structures resulted from the DFT calculations; (a) pure Pt (111), (b) PtAg (111), and (c) Au-doped Pt skin layers supported on the PtAg (111). The oxygen binding energies (E_b) calculated for each model are shown together.

The ORR activity is first evaluated by considering the oxygen binding energy, E_b, which is expressed by:

$$E_b = E_{Slab/O} - E_{Slab} - E_O, \quad (1)$$

where $E_{Slab/O}$, E_{Slab}, and E_O are the total energy of the slab on which atomic O is adsorbed, a clean slab, and the gas-phase O system, respectively. As shown in **Figure 6**, the optimized Au-doped PtAg (E_b = -5.46 eV) surface shows the weaker oxygen binding energy than that of PtAg (E_b = -5.63 eV) and pure Pt (E_b = -5.53 eV) surfaces. This calculation confirms the effectiveness of Au in reducing the binding affinity of the O-containing species on the Pt (111) surface, which has been considered a potential strategy to boost the kinetic activity of Pt-based catalysts [65]. It has been reported that for the surface having weaker oxygen binding energy, the removal of dissociated O adsorbed at the surface is favorable by protonation [66]. Therefore, it is expected that the rate-limiting

step of the ORR is accelerated for the surface with a lower oxygen binding energy, which is, in fact, reflected by the theoretical prediction of the Au-doped PtAg surface in this work. Furthermore, the DFT calculation is in agreement with the experimental results where the improved catalytic activity of Pt-based surface is achieved under the influence of Au doping.

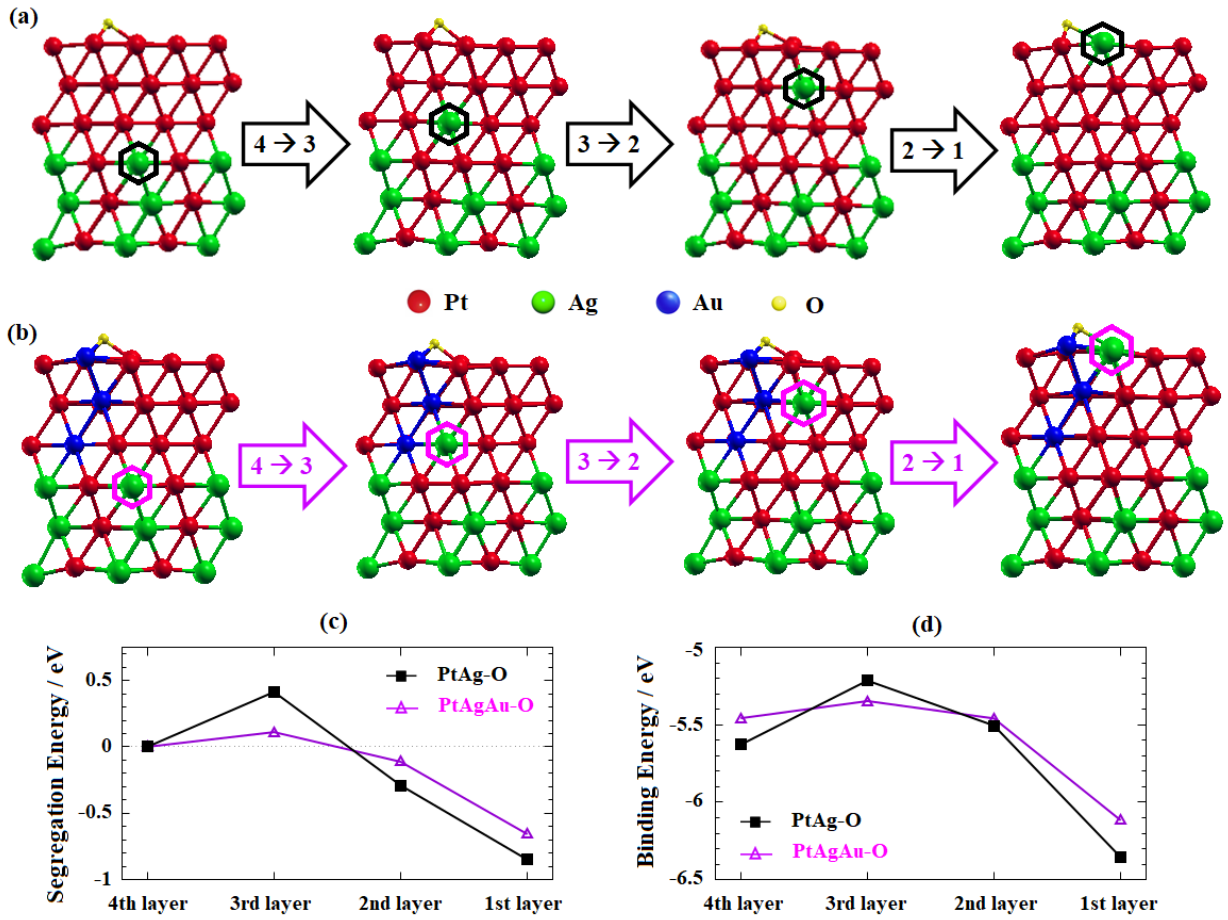

Figure 7. (a). Evolution of the atomic configuration of Ag segregation in (a) PtAg and (b) Au-doped PtAg. (c) The segregation and (d) binding energies as a function of Ag position in PtAg and Au-doped PtAg slabs at oxygen condition.

The durability of Pt-based catalysts was also examined by evaluating the segregation energy for the migration of the Ag atoms on the surface. The segregation energy is calculated by the following equation:

$$\Delta E_{n\to n-1} = E_n - E_{n-1} \quad (2)$$

where n is the vertical position of the Ag atom in the atomic layer of the PtAg or Au-doped PtAg slab (for example, n = 1 indicates the presence of the Ag atom on the first layer), E_n is the total energy of the PtAg or Au-doped PtAg slab when the Ag atom is located at the n^{th} layer under the oxygen-adsorbed condition, and $\Delta E_{n\to n-1}$ is the segregation energy for the migration of the Ag atom in the n^{th} layer toward the $(n\text{-}1)^{th}$ layer.

The optimized structures of the surface with the migration of Ag atoms are shown in

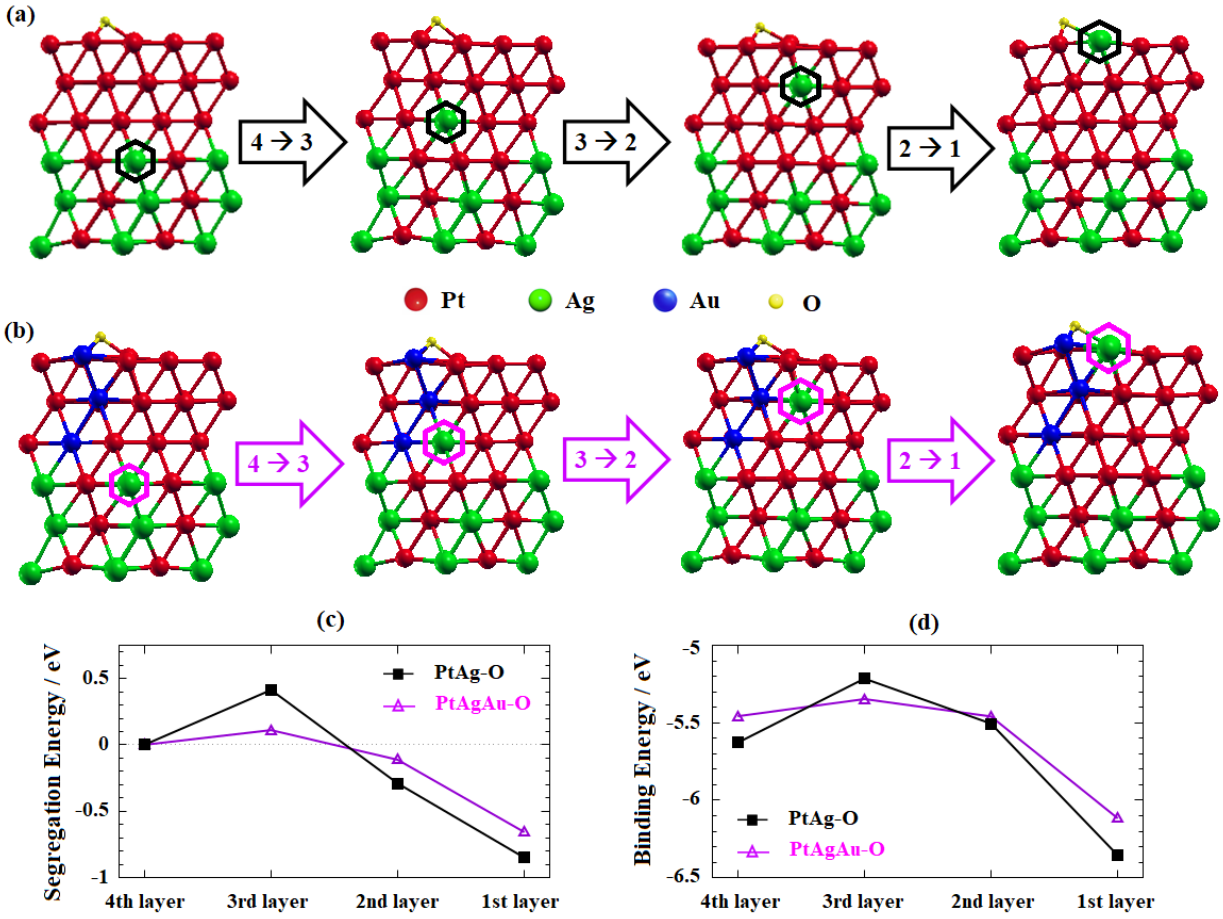

Figure 7a-b for the PtAg or Au-doped PtAg surfaces, respectively. While the calculated segregation energy (ΔE) is shown in

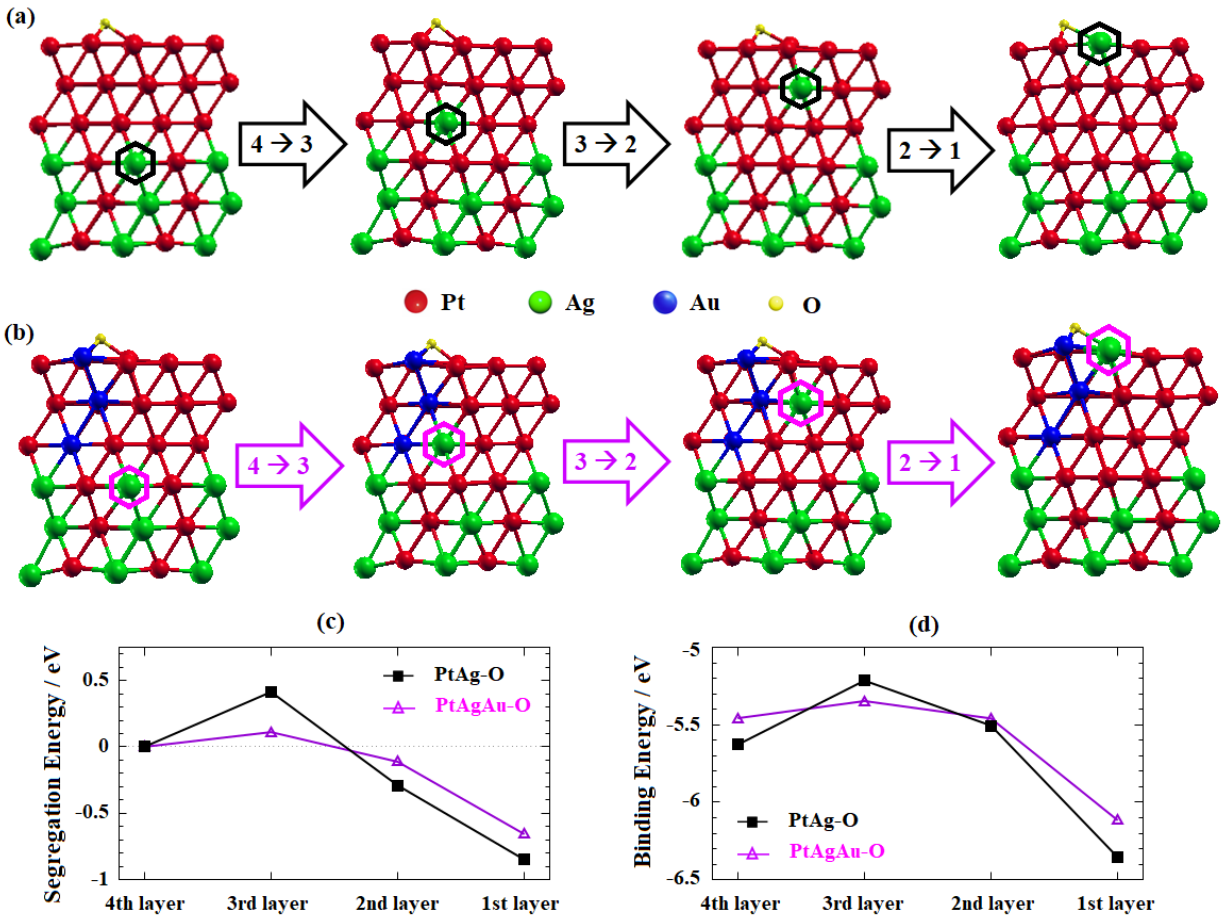

Figure 7c. The positive value of ΔE means that the surface migration of Ag is not favored, while a negative value indicates that the migration is favored [48,67]. Therefore, it is confirmed that the surface migration of Ag is not favored for the migration of Ag atom from the 4th to 3rd layers, while

it is more favored for the migration from the 3rd to the 2nd and the 2nd to the 1st layers (

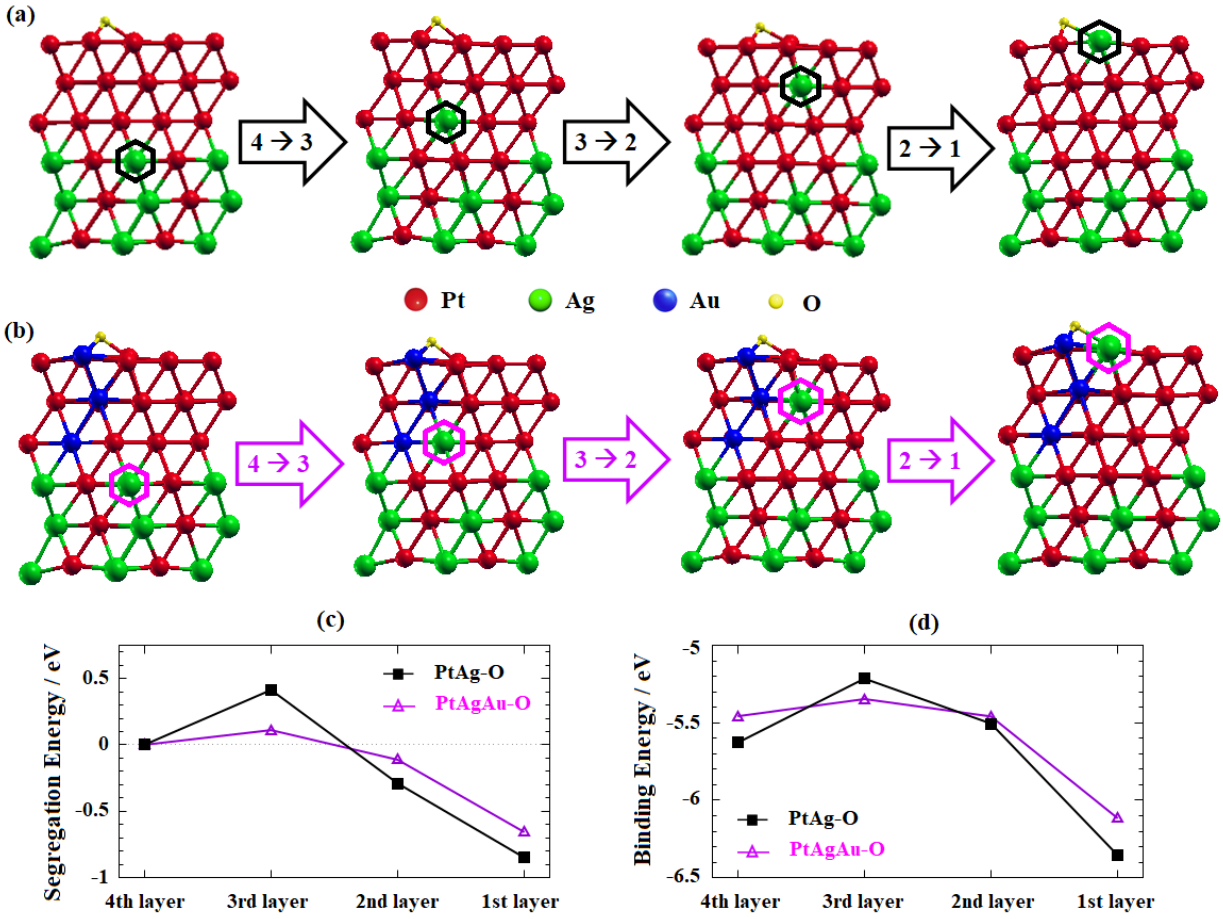

Figure 7c). Importantly, the introduction of Au doping on the PtAg surface enhances the segregation energy for the migration of Ag atom by about 0.2 eV, indicating that Au-doping can suppress the Ag leaching during the ORR. This is also supported by the fact that the migration of the Ag atoms in these layers increases the oxygen binding energy on the surface when the Au

doping is applied (

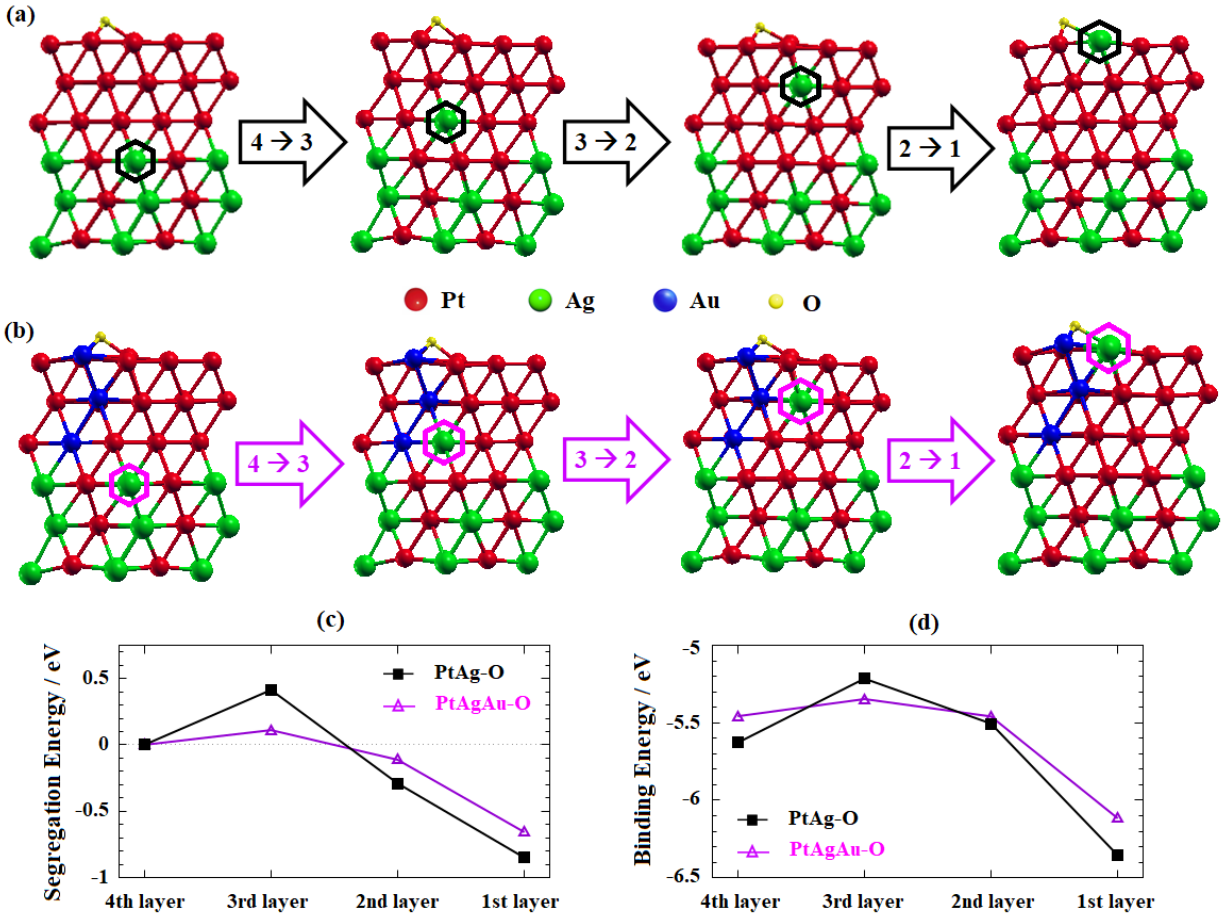

Figure 7d). Accordingly, suppressing the Ag leaching by Au-doping during the ORR effectively enhances the durability of the surface catalyst, which further explains the improved stability of the Au doped PtAg NR array GDE after the ADT compared to that without Au (**Figure 5**).

Therefore, it can be concluded that: the improvement of Au doping on the PtAg NR array GDE can be identified as below: (i) a small amount of Au can effectively control the reduction reaction rate during the NR growth and adjust the atomic arrangement and alloying degree to optimize the active site number on the NR catalyst surface. (ii) The presence of Au weakens the binding of the oxygen species on the catalyst surface, suppressing the segregation of Pt and Ag. Such phenomena

induce the charge transfer effect, which potentially reduces the formation of unstable high-energy Pt sites, improving their stability under ORR conditions.

4. CONCLUSIONS

The development of the hybrid PtAg-Au NR array GDE has been successfully demonstrated via a facile formic acid reduction method, while the presence of 2 at% Au derives the reduction reaction rate leading to harmonized Pt hybrid structure with a high degree deposition of Pt on the NR surface. The MEA test in H_2/Air has shown an enhanced peak power density of 0.61 W cm^{-2}, even with 30% less Pt loading, surpassing the monometallic Pt NR array and commercial Pt/C GDEs. In agreement, the DFT calculation confirms the weakening binding affinity of O-containing species on the Pt surface after the Au doping, which further explains the increased ORR kinetics of the Au doped PtAg NR array GDE. The DFT prediction on Au stabilization effect toward segregation is further approved by the ADT showing significantly improved durability and preventing the ECSA loss of up to ~8 and ~14% less than that of the monometallic Pt NR and PtAg NR array GDE, respectively. These outcomes demonstrate a successful approach to combining the advanced 1D nanostructures and eliminating the carbon support to develop high power performance and durable GDEs.

ASSOCIATED CONTENT

Supporting Information

Results of structure and morphology (TEM and XRD), quantitative composition based on TGA and ICP-MS analyses, additional EIS and MEA testing results, catalytic activities obtained from the single-cell test in H_2/O_2 and the CVs before and after the ADT.

AUTHOR INFORMATION

Corresponding Authors

Elok Fidiani - Department of Physics, Parahyangan Catholic University, Jl. Ciumbuleuit 94, Bandung 40141, Indonesia; orcid.org/0000-0001-5422-1595; Phone: +62 81 222 339 866; E-mail: elokfidiani@unpar.ac.id

Shangfeng Du - School of Chemical Engineering, University of Birmingham, B15 2TT, U.K; orcid.org/0000-0002-4937-6899; Phone: +44 121 4158696; Email: s.du@bham.ac.uk

Authors

Ahmad Zubair AlKahfi - Department of Physics, Universitas Gadjah mada, Kabupaten Sleman, Daerah Istimewa Yogyakarta 55281, Indonesia.

Moh Adhib Ulil Absor - Department of Physics, Universitas Gadjah mada, Kabupaten Sleman, Daerah Istimewa Yogyakarta 55281, Indonesia; orcid.org/0000-0002-4161-4573

Ratna Deca Pravitasari - Research Center for Advanced Materials, National Research and Innovation Agency (BRIN), Building 224, Puspiptek, Tangerang Selatan 15314, Indonesia; orcid.org/0000-0003-1279-0356

Damisih - Research Center for Advanced Materials, National Research and Innovation Agency (BRIN), Building 224, Puspiptek, Tangerang Selatan 15314, Indonesia; orcid.org/0000-0002-0525-5358

Eniya Listiani Dewi - Research Center for Energy Conversion and Conservation, National Research and Innovation Agency (BRIN), Building 620, Puspiptek, Tangerang Selatan 15314, Indonesia.

Gnanavel Thirunavukkarasu - School of Metallurgy and Materials, University of Birmingham, Birmingham, B15 2TT, U.K.

Yulung Chiu - School of Metallurgy and Materials, University of Birmingham, Birmingham, B15 2TT, U.K.

Author Contributions

All authors have given approval to the final version of the manuscript.

Notes

The authors declare no competing financial interest.

ACKNOWLEDGMENT

This work is funded by Lembaga Penelitian dan Pengabdian kepada Masyarakat (LPPM), Parahyangan Catholic University (III/LPPM/2022-02/74-P) and the EPSRC Centre for Doctoral Training in Fuel Cells and their Fuels (EP/L015749/1). The computation in this research was performed using the computer facilities at Universitas Gadjah Mada (UGM) sponsored by UGM through RTA program (No. 3550/UN1.P.III/Dit-Lit/PT.01.05/2022).

REFERENCES

(1) Debe, M. K. Electrocatalyst Approaches and Challenges for Automotive Fuel Cells. *Nature*. June 7, 2012, pp 43–51. https://doi.org/10.1038/nature11115.

(2) Kongkanand, A.; Mathias, M. F. The Priority and Challenge of High-Power Performance of Low-Platinum Proton-Exchange Membrane Fuel Cells. *Journal of Physical Chemistry Letters*. American Chemical Society April 21, 2016, pp 1127–1137. https://doi.org/10.1021/acs.jpclett.6b00216.

(3) Čolić, V.; Bandarenka, A. S. Pt Alloy Electrocatalysts for the Oxygen Reduction Reaction: From Model Surfaces to Nanostructured Systems. *ACS Catal*. **2016**, *6* (8), 5378–5385. https://doi.org/10.1021/acscatal.6b00997.

(4) Jia, Q.; Liang, W.; Bates, M. K.; Mani, P.; Lee, W.; Mukerjee, S. Activity Descriptor Identification for Oxygen Reduction on Platinum-Based Bimetallic Nanoparticles: In Situ Observation of the Linear Composition-Strain-Activity Relationship. *ACS Nano* **2015**, *9* (1), 387–400. https://doi.org/10.1021/nn506721f.

(5) Wang, D.; Xin, H. ordered intermetallic platinum-cobalt core-shell nanoparticles with enhanced activity and stability as oxygen reduction electrocatalystsn L.; Hovden, R.; Wang, H.; Yu, Y.; Muller, D. A.; Disalvo, F. J.; Abruña, H. D. Structurally Ordered Intermetallic Platinum-Cobalt Core-Shell Nanoparticles with Enhanced Activity and Stability as Oxygen Reduction Electrocatalysts. *Nat. Mater*. **2013**, *12* (1), 81–87. https://doi.org/10.1038/nmat3458.

(6) Chong, L.; Wen, J.; Kubal, J.; Sen, F. G.; Zou, J.; Greeley, J.; Chan, M.; Barkholtz, H.; Ding, W.; Liu, D. J. Ultralow-Loading Platinum-Cobalt Fuel Cell Catalysts Derived from

Imidazolate Frameworks. *Science (80-.).* **2018**, *362* (6420), 1276–1281. https://doi.org/10.1126/science.aau0630.

(7) Bu, L.; Guo, S.; Zhang, X.; Shen, X.; Su, D.; Lu, G.; Zhu, X.; Yao, J.; Guo, J.; Huang, X. Surface Engineering of Hierarchical Platinum-Cobalt Nanowires for Efficient Electrocatalysis. *Nat. Commun.* **2016**, *7* (1), 1–10. https://doi.org/10.1038/ncomms11850.

(8) Huang, X.; Zhu, E.; Chen, Y.; Li, Y.; Chiu, C. Y.; Xu, Y.; Lin, Z.; Duan, X.; Huang, Y. A Facile Strategy to Pt3Ni Nanocrystals with Highly Porous Features as an Enhanced Oxygen Reduction Reaction Catalyst. *Adv. Mater.* **2013**, *25* (21), 2974–2979. https://doi.org/10.1002/adma.201205315.

(9) Stamenkovic, V. R.; Fowler, B.; Mun, B. S.; Wang, G.; Ross, P. N.; Lucas, C. A.; Markovic, N. M. Improved Oxygen Reduction Activity on Pt3Ni(111) via Increased Surface Site Availability. *Science (80-.).* **2007**, *315* (5811), 493–497. https://doi.org/10.1126/science.1135941.

(10) Bu, L.; Ding, J.; Guo, S.; Zhang, X.; Su, D.; Zhu, X.; Yao, J.; Guo, J.; Lu, G.; Huang, X. A General Method for Multimetallic Platinum Alloy Nanowires as Highly Active and Stable Oxygen Reduction Catalysts. *Adv. Mater.* **2015**, *27* (44), 7204–7212. https://doi.org/10.1002/adma.201502725.

(11) Chung, Y. H.; Chung, D. Y.; Jung, N.; Park, H. Y.; Sung, Y. E.; Yoo, S. J. Effect of Surface Composition of Pt-Fe Nanoparticles for Oxygen Reduction Reactions. *Int. J. Hydrogen Energy* **2014**, *39* (27), 14751–14759. https://doi.org/10.1016/j.ijhydene.2014.07.097.

(12) Chung, D. Y.; Jun, S. W.; Yoon, G.; Kwon, S. G.; Shin, D. Y.; Seo, P.; Yoo, J. M.; Shin, H.; Chung, Y. H.; Kim, H.; Mun, B. S.; Lee, K. S.; Lee, N. S.; Yoo, S. J.; Lim, D. H.; Kang, K.;

Sung, Y. E.; Hyeon, T. Highly Durable and Active PtFe Nanocatalyst for Electrochemical Oxygen Reduction Reaction. *J. Am. Chem. Soc.* **2015**, *137* (49), 15478–15485. https://doi.org/10.1021/jacs.5b09653.

(13) Wang, C.; Van Der Vliet, D.; More, K. L.; Zaluzec, N. J.; Peng, S.; Sun, S.; Daimon, H.; Wang, G.; Greeley, J.; Pearson, J.; Paulikas, A. P.; Karapetrov, G.; Strmcnik, D.; Markovic, N. M.; Stamenkovic, V. R. Multimetallic Au/FePt3 Nanoparticles as Highly Durable Electrocatalyst. *Nano Lett.* **2011**, *11* (3), 919–926. https://doi.org/10.1021/nl102369k.

(14) Lu, Y.; Du, S.; Steinberger-Wilckens, R. Three-Dimensional Catalyst Electrodes Based on PtPd Nanodendrites for Oxygen Reduction Reaction in PEFC Applications. *Appl. Catal. B Environ.* **2016**, *187*, 108–114. https://doi.org/10.1016/j.apcatb.2016.01.019.

(15) Choi, S. Il; Shao, M.; Lu, N.; Ruditskiy, A.; Peng, H. C.; Park, J.; Guerrero, S.; Wang, J.; Kim, M. J.; Xia, Y. Synthesis and Characterization of Pd@Pt-Ni Core-Shell Octahedra with High Activity toward Oxygen Reduction. *ACS Nano* **2014**, *8* (10), 10363–10371. https://doi.org/10.1021/nn5036894.

(16) Liang, Y.; Lin, S.; Liu, C.; Chung, S.; Chen, T.; Wang, J.-H.; Wang, K. The Performance and Stability of the Oxygen Reduction Reaction on Pt–M (M = Pd, Ag and Au) Nanorods: An Experimental and Computational Study. *Chem. Commun.* **2015**, *51* (30), 6605–6608. https://doi.org/10.1039/C5CC01629K.

(17) Kang, Y.; Snyder, J.; Chi, M.; Li, D.; More, K. L.; Markovic, N. M.; Stamenkovic, V. R. Multimetallic Core/Interlayer/Shell Nanostructures as Advanced Electrocatalysts. *Nano Lett.* **2014**, *14* (11), 6361–6367. https://doi.org/10.1021/nl5028205.

(18) Esfandiari, A.; Kazemeini, M.; Bastani, D. Synthesis, Characterization and Performance Determination of an Ag@Pt/C Electrocatalyst for the ORR in a PEM Fuel Cell. *Int. J. Hydrogen Energy* **2016**, *41* (45), 20720–20730. https://doi.org/10.1016/j.ijhydene.2016.09.097.

(19) Liu, H.; Ye, F.; Yao, Q.; Cao, H.; Xie, J.; Lee, J. Y.; Yang, J. Stellated Ag-Pt Bimetallic Nanoparticles: An Effective Platform for Catalytic Activity Tuning. *Sci. Rep.* **2014**, *4* (1), 1–7. https://doi.org/10.1038/srep03969.

(20) Fu, T.; Fang, J.; Wang, C.; Zhao, J. Hollow Porous Nanoparticles with Pt Skin on a Ag-Pt Alloy Structure as a Highly Active Electrocatalyst for the Oxygen Reduction Reaction. *J. Mater. Chem. A* **2016**, *4* (22), 8803–8811. https://doi.org/10.1039/c6ta02202b.

(21) Yoshida, T.; Kojima, K. Toyota MIRAI Fuel Cell Vehicle and Progress toward a Future Hydrogen Society. *Electrochem. Soc. Interface* **2015**, *24* (2), 45–49. https://doi.org/10.1149/2.F03152if.

(22) Ferreira, P. J.; la O', G. J.; Shao-Horn, Y.; Morgan, D.; Makharia, R.; Kocha, S.; Gasteiger, H. A. Instability of Pt/C Electrocatalysts in Proton Exchange Membrane Fuel Cells. *J. Electrochem. Soc.* **2005**, *152* (11), A2256. https://doi.org/10.1149/1.2050347.

(23) Shao, Y.; Yin, G.; Gao, Y. Understanding and Approaches for the Durability Issues of Pt-Based Catalysts for PEM Fuel Cell. *Journal of Power Sources*. Elsevier September 27, 2007, pp 558–566. https://doi.org/10.1016/j.jpowsour.2007.07.004.

(24) Chung, D. Y.; Yoo, J. M.; Sung, Y.-E. Highly Durable and Active Pt-Based Nanoscale Design for Fuel-Cell Oxygen-Reduction Electrocatalysts. *Adv. Mater.* **2018**, *30* (42), 1704123. https://doi.org/10.1002/adma.201704123.

(25) Macauley, N.; Papadias, D. D.; Fairweather, J.; Spernjak, D.; Langlois, D.; Ahluwalia, R.; More, K. L.; Mukundan, R.; Borup, R. L. Carbon Corrosion in PEM Fuel Cells and the Development of Accelerated Stress Tests. *J. Electrochem. Soc.* **2018**, *165* (6), F3148–F3160. https://doi.org/10.1149/2.0061806jes.

(26) Dubau, L.; Castanheira, L.; Maillard, F.; Chatenet, M.; Lottin, O.; Maranzana, G.; Dillet, J.; Lamibrac, A.; Perrin, J. C.; Moukheiber, E.; Elkaddouri, A.; De Moor, G.; Bas, C.; Flandin, L.; Caqué, N. A Review of PEM Fuel Cell Durability: Materials Degradation, Local Heterogeneities of Aging and Possible Mitigation Strategies. *Wiley Interdisciplinary Reviews: Energy and Environment*. John Wiley and Sons Ltd November 1, 2014, pp 540–560. https://doi.org/10.1002/wene.113.

(27) Maillard, F.; O. Silva, W.; Castanheira, L.; Dubau, L.; Lima, F. H. B. Carbon Corrosion in Proton-Exchange Membrane Fuel Cells: Spectrometric Evidence for Pt-Catalysed Decarboxylation at Anode-Relevant Potentials. *ChemPhysChem* **2019**, *20* (22), 3106–3111. https://doi.org/10.1002/cphc.201900505.

(28) Chen, S.; Gasteiger, H. A.; Hayakawa, K.; Tada, T.; Shao-Horn, Y. Platinum-Alloy Cathode Catalyst Degradation in Proton Exchange Membrane Fuel Cells: Nanometer-Scale Compositional and Morphological Changes. *J. Electrochem. Soc.* **2010**, *157* (1), A82. https://doi.org/10.1149/1.3258275.

(29) Dubau, L.; Lopez-Haro, M.; Castanheira, L.; Durst, J.; Chatenet, M.; Bayle-Guillemaud, P.; Guétaz, L.; Caqué, N.; Rossinot, E.; Maillard, F. Probing the Structure, the Composition and the ORR Activity of Pt3Co/C Nanocrystallites during a 3422h PEMFC Ageing Test. *Appl. Catal. B Environ.* **2013**, *142–143*, 801–808. https://doi.org/10.1016/j.apcatb.2013.06.011.

(30) Cui, C.; Gan, L.; Heggen, M.; Rudi, S.; Strasser, P. Compositional Segregation in Shaped Pt Alloy Nanoparticles and Their Structural Behaviour during Electrocatalysis. *Nat. Mater.* **2013**, *12* (8), 765–771. https://doi.org/10.1038/nmat3668.

(31) Wang, Y. J.; Zhao, N.; Fang, B.; Li, H.; Bi, X. T.; Wang, H. Carbon-Supported Pt-Based Alloy Electrocatalysts for the Oxygen Reduction Reaction in Polymer Electrolyte Membrane Fuel Cells: Particle Size, Shape, and Composition Manipulation and Their Impact to Activity. *Chemical Reviews*. American Chemical Society 2015, pp 3433–3467. https://doi.org/10.1021/cr500519c.

(32) Shao, M.; Chang, Q.; Dodelet, J. P.; Chenitz, R. Recent Advances in Electrocatalysts for Oxygen Reduction Reaction. *Chemical Reviews*. American Chemical Society March 23, 2016, pp 3594–3657. https://doi.org/10.1021/acs.chemrev.5b00462.

(33) Viswanathan, V.; Hansen, H. A.; Rossmeisl, J.; Nørskov, J. K. Universality in Oxygen Reduction Electrocatalysis on Metal Surfaces. *ACS Catal.* **2012**, *2* (8), 1654–1660. https://doi.org/10.1021/cs300227s.

(34) Xia, Y.; Yang, P.; Sun, Y.; Wu, Y.; Mayers, B.; Gates, B.; Yin, Y.; Kim, F.; Yan, H. One-Dimensional Nanostructures: Synthesis, Characterization, and Applications. *Advanced Materials*. John Wiley & Sons, Ltd March 4, 2003, pp 353–389. https://doi.org/10.1002/adma.200390087.

(35) Cademartiri, L.; Ozin, G. A. Ultrathin Nanowires—A Materials Chemistry Perspective. *Adv. Mater.* **2009**, *21* (9), 1013–1020. https://doi.org/10.1002/adma.200801836.

(36) Lu, Y.; Du, S.; Steinberger-Wilckens, R. One-Dimensional Nanostructured Electrocatalysts for Polymer Electrolyte Membrane Fuel Cells—A Review. *Applied Catalysis B:*

Environmental. Elsevier B.V. December 15, 2016, pp 292–314. https://doi.org/10.1016/j.apcatb.2016.06.022.

(37) Jiang, K.; Zhao, D.; Guo, S.; Zhang, X.; Zhu, X.; Guo, J.; Lu, G.; Huang, X. Efficient Oxygen Reduction Catalysis by Subnanometer Pt Alloy Nanowires. *Sci. Adv.* **2017**, *3* (2), e1601705. https://doi.org/10.1126/sciadv.1601705.

(38) Li, M.; Zhao, Z.; Cheng, T.; Fortunelli, A.; Chen, C. Y.; Yu, R.; Zhang, Q.; Gu, L.; Merinov, B. V.; Lin, Z.; Zhu, E.; Yu, T.; Jia, Q.; Guo, J.; Zhang, L.; Goddard, W. A.; Huang, Y.; Duan, X. Ultrafine Jagged Platinum Nanowires Enable Ultrahigh Mass Activity for the Oxygen Reduction Reaction. *Science (80-.).* **2016**, *354* (6318), 1414–1419. https://doi.org/10.1126/science.aaf9050.

(39) Safo, I. A.; Dosche, C.; Özaslan, M. Effects of Capping Agents on the Oxygen Reduction Reaction Activity and Shape Stability of Pt Nanocubes. *ChemPhysChem* **2019**, *20* (22), 3010–3023. https://doi.org/10.1002/CPHC.201900653.

(40) Pan, L.; Ott, S.; Dionigi, F.; Strasser, P. Current Challenges Related to the Deployment of Shape-Controlled Pt Alloy Oxygen Reduction Reaction Nanocatalysts into Low Pt-Loaded Cathode Layers of Proton Exchange Membrane Fuel Cells. *Current Opinion in Electrochemistry*. Elsevier B.V. December 1, 2019, pp 61–71. https://doi.org/10.1016/j.coelec.2019.10.011.

(41) Hoshi, Y.; Yoshida, T.; Nishikata, A.; Tsuru, T. Dissolution of Pt-M (M: Cu, Co, Ni, Fe) Binary Alloys in Sulfuric Acid Solution. *Electrochim. Acta* **2011**, *56* (15), 5302–5309. https://doi.org/10.1016/j.electacta.2011.04.007.

(42) Ma, Y.; Balbuena, P. B. Pt Surface Segregation in Bimetallic Pt3M Alloys: A Density Functional Theory Study. *Surf. Sci.* **2008**, *602* (1), 107–113. https://doi.org/10.1016/j.susc.2007.09.052.

(43) Schlapka, A.; Lischka, M.; Groß, A.; Käsberger, U.; Jakob, P. Surface Strain versus Substrate Interaction in Heteroepitaxial Metal Layers: Pt on Ru(0001). *Phys. Rev. Lett.* **2003**, *91* (1), 016101/1-016101/4. https://doi.org/10.1103/PhysRevLett.91.016101.

(44) Jia, Q.; Segre, C. U.; Ramaker, D.; Caldwell, K.; Trahan, M.; Mukerjee, S. Structure-Property-Activity Correlations of Pt-Bimetallic Nanoparticles: A Theoretical Study. *Electrochim. Acta* **2013**, *88*, 604–613. https://doi.org/10.1016/j.electacta.2012.10.124.

(45) Ruban, A.; Hammer, B.; Stoltze, P.; Skriver, H. L.; Nørskov, J. K. Surface Electronic Structure and Reactivity of Transition and Noble Metals. In *Journal of Molecular Catalysis A: Chemical*; Elsevier, 1997; Vol. 115, pp 421–429. https://doi.org/10.1016/S1381-1169(96)00348-2.

(46) Zhang, J.; Sasaki, K.; Sutter, E.; Adzic, R. R. Stabilization of Platinum Oxygen-Reduction Electrocatalysts Using Gold Clusters. *Science (80-.).* **2007**, *315* (5809), 220–222. https://doi.org/10.1126/science.1134569.

(47) Gatalo, M.; Jovanovič, P.; Polymeros, G.; Grote, J.-P.; Pavlišič, A.; Ruiz- Zepeda, F.; Šelih, V. S.; Šala, M.; Hočevar, S.; Bele, M.; Mayrhofer, K. J. J.; Hodnik, N.; Gaberšček, M. Positive Effect of Surface Doping with Au on the Stability of Pt-Based Electrocatalysts. *ACS Catal.* **2016**, *6* (3), 1630–1634. https://doi.org/10.1021/acscatal.5b02883.

(48) Choi, J.; Cho, J.; Roh, C. W.; Kim, B. S.; Choi, M. S.; Jeong, H.; Ham, H. C.; Lee, H. Au-Doped PtCo/C Catalyst Preventing Co Leaching for Proton Exchange Membrane Fuel Cells. *Appl. Catal. B Environ.* **2019**, *247*, 142–149. https://doi.org/10.1016/j.apcatb.2019.02.002.

(49) Dorjgotov, A.; Jeon, Y.; Hwang, J.; Ulziidelger, B.; Kim, H. S.; Han, B.; Shul, Y. G. Synthesis of Durable Small-Sized Bilayer Au@Pt Nanoparticles for High Performance PEMFC Catalysts. *Electrochim. Acta* **2017**, *228*, 389–397. https://doi.org/10.1016/j.electacta.2017.01.083.

(50) Fidiani, E.; Thirunavukkarasu, G.; Li, Y.; Chiu, Y.-L.; Du, S. Au Integrated AgPt Nanorods for Oxygen Reduction Reaction in Proton Exchange Membrane Fuel Cells. *J. Mater. Chem. A* **2021**. https://doi.org/10.1039/d0ta08551k.

(51) Fidiani, E.; Thirunavukkarasu, G.; Li, Y.; Chiu, Y.-L.; Du, S. Ultrathin AgPt Alloy Nanorods as Low-Cost Oxygen Reduction Reaction Electrocatalysts in Proton Exchange Membrane Fuel Cells. *J. Mater. Chem. A* **2020**, *8* (23), 11874–11883. https://doi.org/10.1039/D0TA02748K.

(52) Hung, C. C.; Lim, P. Y.; Chen, J. R.; Shih, H. C. Corrosion of Carbon Support for PEM Fuel Cells by Electrochemical Quartz Crystal Microbalance. *J. Power Sources* **2011**. https://doi.org/10.1016/j.jpowsour.2010.07.015.

(53) Holdcroft, S. Fuel Cell Catalyst Layers: A Polymer Science Perspective. *Chemistry of Materials*. January 14, 2014, pp 381–393. https://doi.org/10.1021/cm401445h.

(54) Lu, Y.; Du, S.; Steinberger-Wilckens, R. Temperature-Controlled Growth of Single-Crystal Pt Nanowire Arrays for High Performance Catalyst Electrodes in Polymer Electrolyte Fuel Cells. *Appl. Catal. B Environ.* **2015**, *164*, 389–395. https://doi.org/10.1016/j.apcatb.2014.09.040.

(55) Tsotridis, G.; Pilenga, A.; Marco, G. De; Malkow, T. *EU Harmonised Test Protocols for PEMFC MEA Testing in Single Cell Configuration for Automotive Applications; JRC Science for Policy Report*; 2015. https://doi.org/10.2790/54653.

(56) Mardle, P.; Thirunavukkarasu, G.; Guan, S.; Chiu, Y. L.; Du, S. Comparative Study of PtNi Nanowire Array Electrodes toward Oxygen Reduction Reaction by Half-Cell Measurement and PEMFC Test. *ACS Appl. Mater. Interfaces* **2020**, *12* (38), 42832–42841. https://doi.org/10.1021/acsami.0c11531.

(57) Fang, C.; Zhao, J.; Zhao, G.; Kuai, L.; Geng, B. Simultaneous Tunable Structure and Composition of PtAg Alloyed Nanocrystals as Superior Catalysts. *Nanoscale* **2016**, *8* (32), 14971–14978. https://doi.org/10.1039/c6nr02643e.

(58) Hansen, H. A.; Rossmeisl, J.; Nørskov, J. K. Surface Pourbaix Diagrams and Oxygen Reduction Activity of Pt, Ag and Ni(111) Surfaces Studied by DFT. *Phys. Chem. Chem. Phys.* **2008**, *10* (25), 3722–3730. https://doi.org/10.1039/b803956a.

(59) Troullier, N.; Martins, J. L. Efficient Pseudopotentials for Plane-Wave Calculations. *Phys. Rev. B* **1991**, *43* (3), 1993. https://doi.org/10.1103/PhysRevB.43.1993.

(60) Ozaki, T. Variationally Optimized Atomic Orbitals for Large-Scale Electronic Structures. *Phys. Rev. B* **2003**, *67* (15), 155108. https://doi.org/10.1103/PhysRevB.67.155108.

(61) Ozaki, T.; Kino, H. Efficient Projector Expansion for the Ab Initio LCAO Method. *Phys. Rev. B - Condens. Matter Mater. Phys.* **2005**, *72* (4), 045121. https://doi.org/10.1103/PHYSREVB.72.045121/FIGURES/3/MEDIUM.

(62) Ozaki, T.; Kino, H. Numerical Atomic Basis Orbitals from H to Kr. *Phys. Rev. B* **2004**, *69* (19), 195113. https://doi.org/10.1103/PhysRevB.69.195113.

(63) Perdew, J. P.; Burke, K.; Ernzerhof, M. Generalized Gradient Approximation Made Simple. *Phys. Rev. Lett.* **1996**, *77* (18), 3865. https://doi.org/10.1103/PhysRevLett.77.3865.

(64) Kohn, W.; Sham, L. J. Self-Consistent Equations Including Exchange and Correlation Effects. *Phys. Rev.* **1965**, *140* (4A), A1133. https://doi.org/10.1103/PHYSREV.140.A1133/FIGURE/1/THUMB.

(65) Stamenkovic, V.; Mun, B. S.; Mayrhofer, K. J. J.; Ross, P. N.; Markovic, N. M.; Rossmeisl, J.; Greeley, J.; Nørskov, J. K. Changing the Activity of Electrocatalysts for Oxygen Reduction by Tuning the Surface Electronic Structure. *Angew. Chem. Int. Ed. Engl.* **2006**, *45* (18), 2897–2901. https://doi.org/10.1002/anie.200504386.

(66) Nørskov, J. K.; Rossmeisl, J.; Logadottir, A.; Lindqvist, L.; Kitchin, J. R.; Bligaard, T.; Jónsson, H. Origin of the Overpotential for Oxygen Reduction at a Fuel-Cell Cathode. *J. Phys. Chem. B* **2004**, *108* (46), 17886–17892. https://doi.org/10.1021/jp047349j.

(67) Ham, H. C.; Manogaran, D.; Lee, K. H.; Kwon, K.; Jin, S. A.; You, D. J.; Pak, C.; Hwang, G. S. Communication: Enhanced Oxygen Reduction Reaction and Its Underlying Mechanism in Pd-Ir-Co Trimetallic Alloys. *J. Chem. Phys.* **2013**, *139* (20). https://doi.org/10.1063/1.4837176.

Graphical Abstract

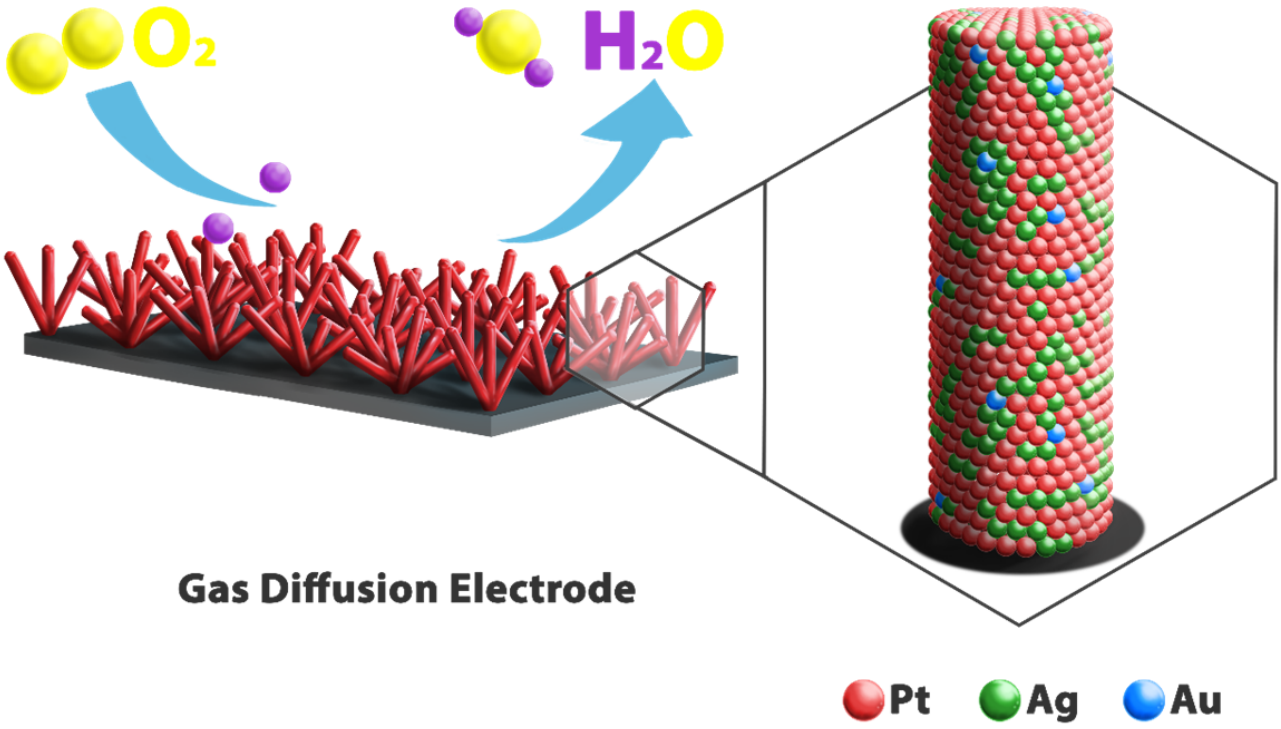

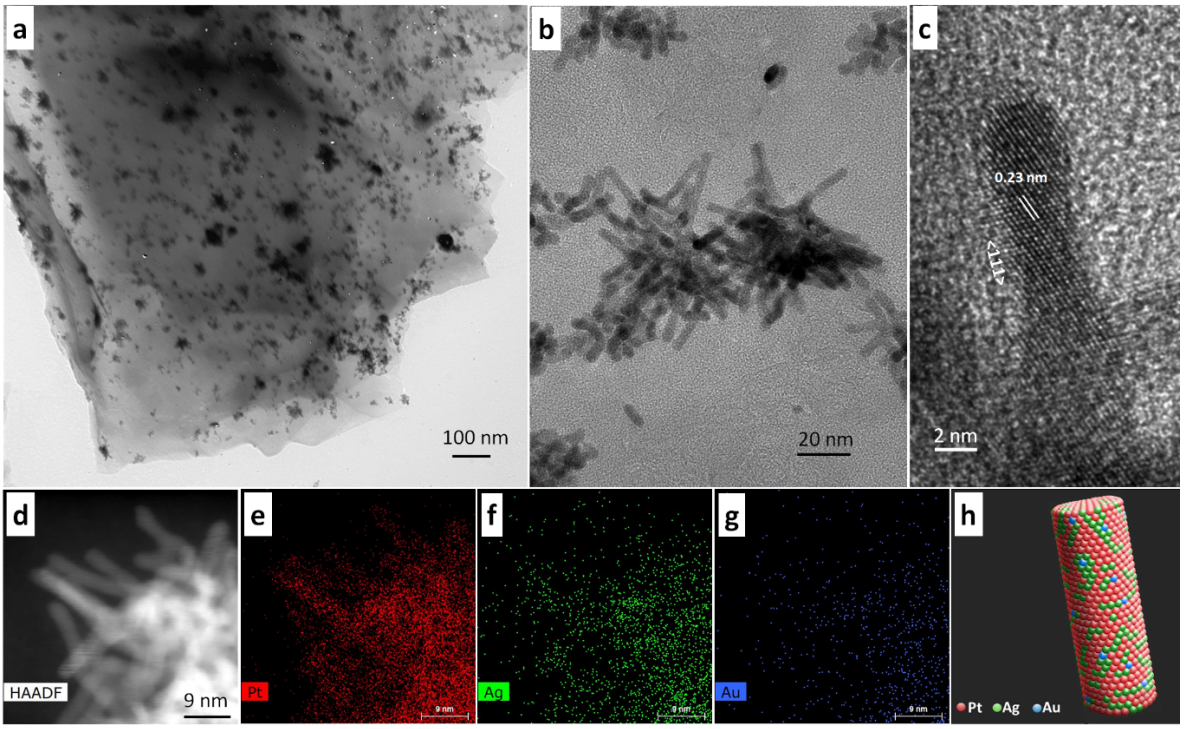

Figure 8. Images of PtAg-Au NR array GDE obtained by (a-b) TEM, (c) HR-TEM, (d-g) the element mapping by STEM-EDX and (h) a visualized structure of PtAg-Au NR.

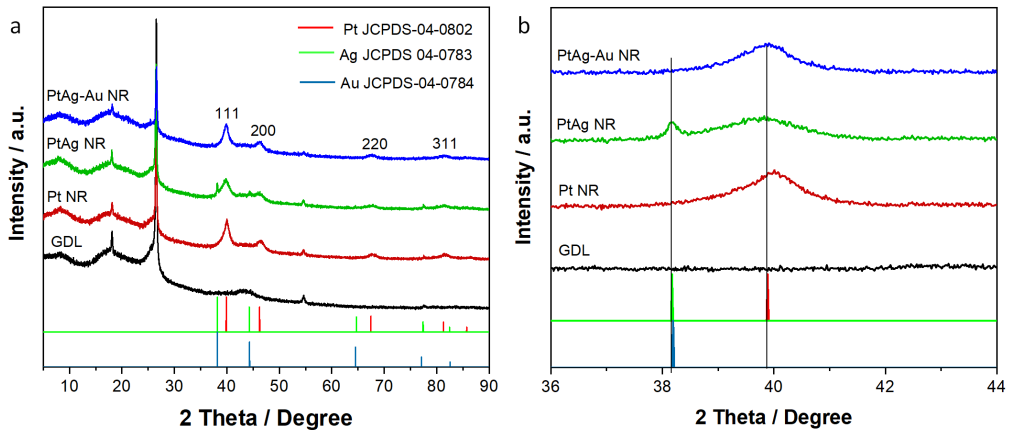

Figure 9. XRD patterns of the Pt NR, PtAg NR and PtAg-Au NR array GDEs with the references of bulk Pt, Ag and Au and GDL.

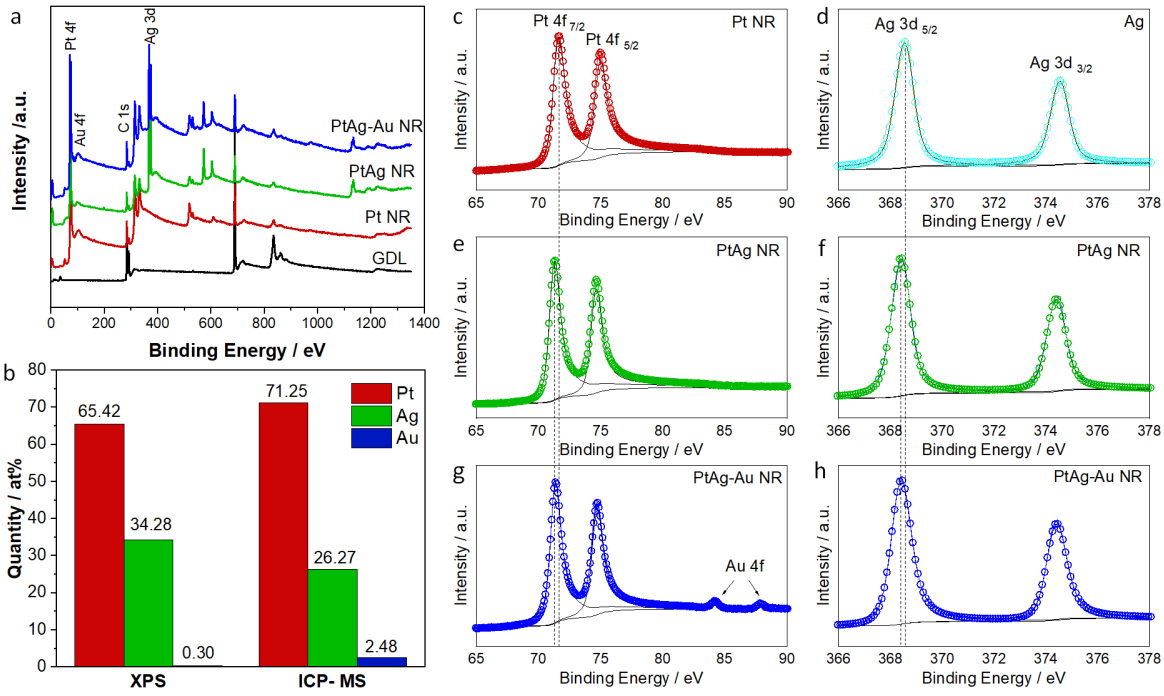

Figure 10. (a) XPS survey of the GDL, Pt NR, PtAg NR and PtAg-Au NR array GDEs, (b) comparison of quantitative measurement of PtAg-Au NR using XPS and ICP-MS analyses. (c-h) High-resolution XPS spectra of Pt 4f and Ag 3d regions of the as-made GDEs.

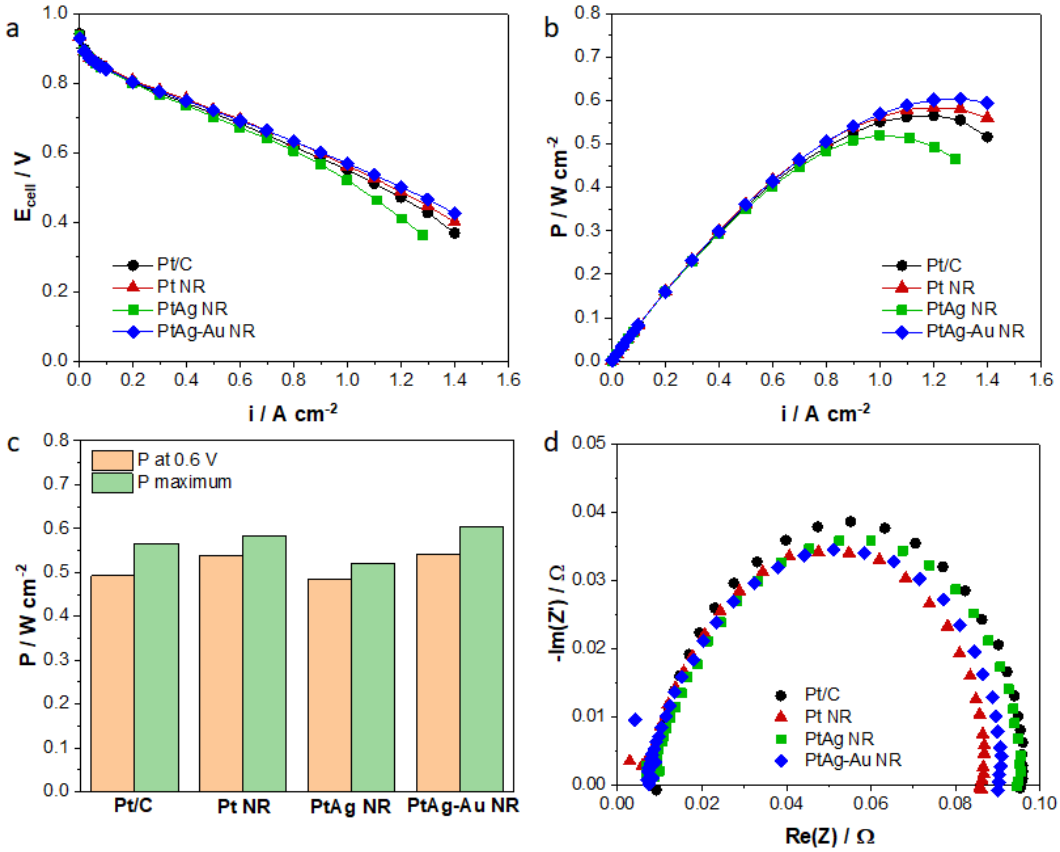

Figure 11. MEA testing results obtained under fully humidified H2/air at 80 °C with stoichiometric ratios of 1.3/1.5 and absolute pressure of 2.5/2.3 bar_{abs}, respectively: (a) polarization and (b) power density curves of the commercial Pt/C, Pt NR, PtAg NR and PtAg-Au NR array GDEs. (c) Comparison of the corresponding peak and power density at 0.6 V and (d) the corresponding EIS spectra recorded at 30 mA cm^{-2}.

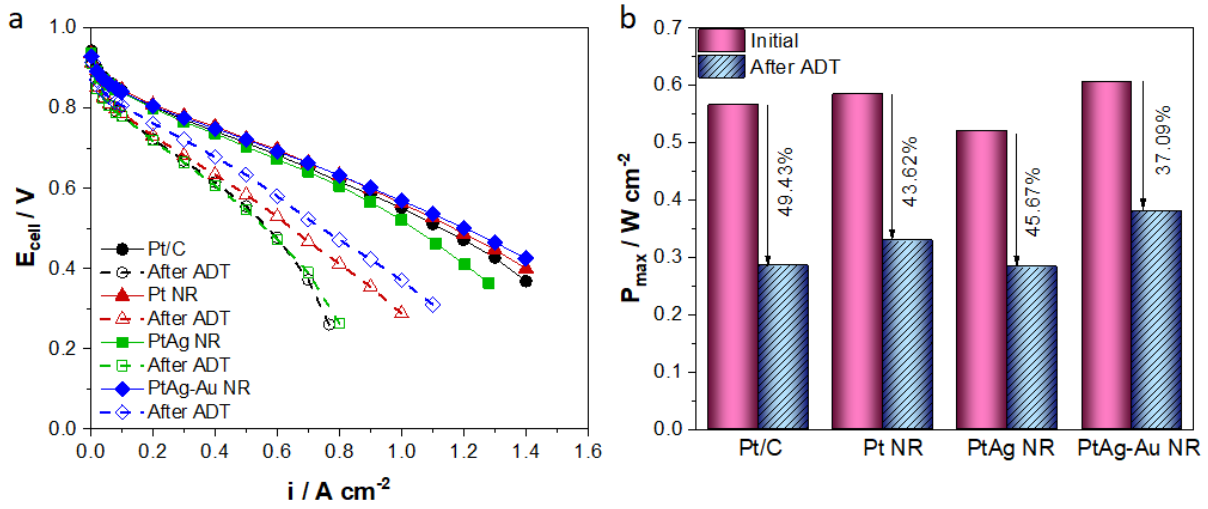

Figure 12. (a) Comparison of polarization curves and (b) the corresponding power density decline ratio from different GDEs after the ADT recorded under fully humidified H_2/air at 80 °C with stoichiometric ratios of 1.3/1.5 and absolute pressure of 2.5/2.3 bar_{abs}, respectively.

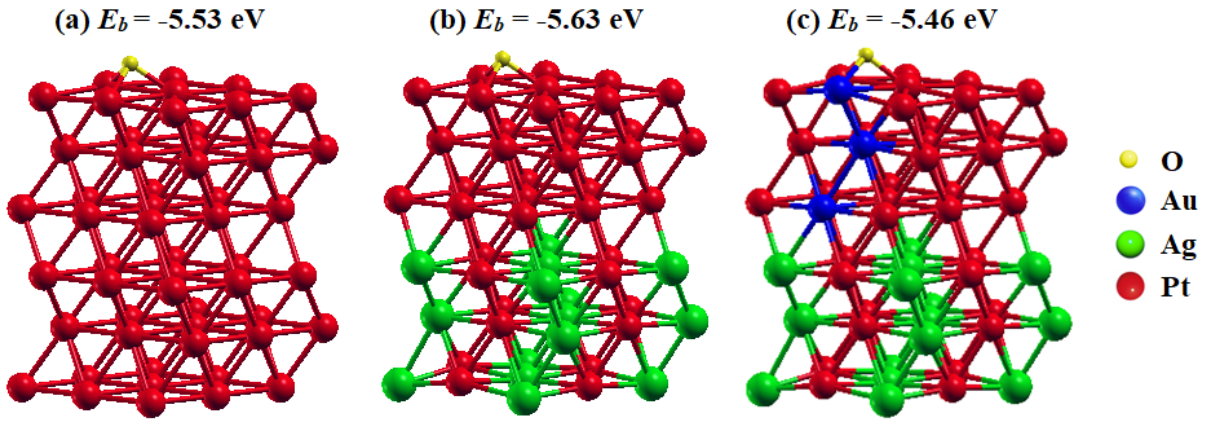

Figure 13. (a) Optimized atomic structures resulted from the DFT calculations; (a) pure Pt (111), (b) PtAg (111), and (c) Au-doped Pt skin layers supported on the PtAg (111). The oxygen binding energies (E_b) calculated for each model are shown together.

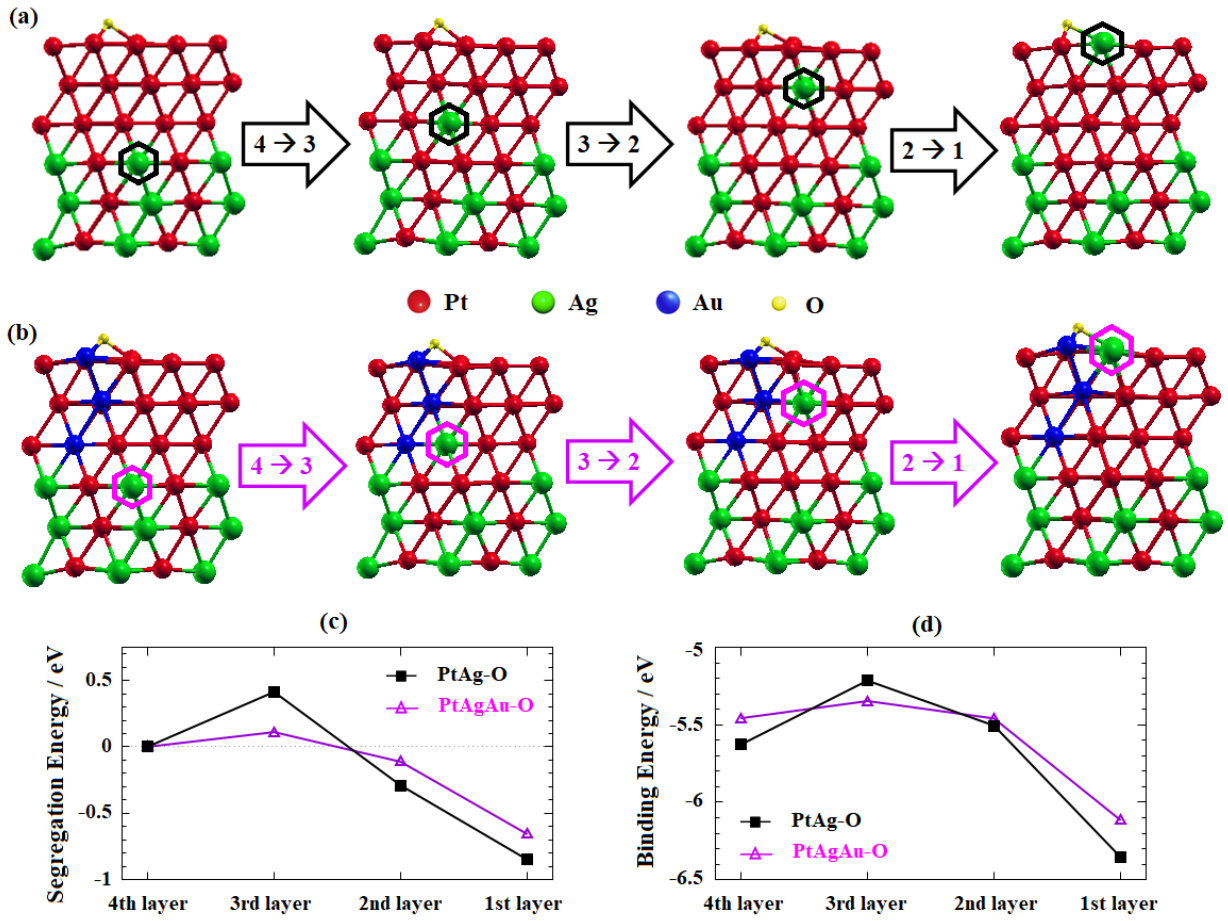

Figure 14. (a). Evolution of the atomic configuration of Ag segregation in (a) PtAg and (b) Au-doped PtAg. (c) The segregation and (d) binding energies as a function of Ag position in PtAg and Au-doped PtAg slabs at oxygen condition.